Title
Methods for hydrographic data collection and use applied to infer biogeochemistry in the Southern Ocean

Permalink
https://escholarship.org/uc/item/39b0j1tc

Author
Carter, Brendan Rae

Publication Date
2011

Peer reviewed|Thesis/dissertation

UNIVERSITY OF CALIFORNIA, SAN DIEGO

Methods for Hydrographic Data Collection and Use
Applied to Infer Biogeochemistry in the Southern Ocean

A dissertation submitted in partial satisfaction of the requirements for the degree Doctor
of Philosophy

in

Oceanography

by

Brendan Rae Carter

Committee in charge:

      Professor Andrew Dickson, Chair
      Professor Ralph Keeling
      Professor Jeffrey Severinghaus
      Professor Lynne Talley
      Professor William Trogler

2011

The Dissertation of Brendan Rae Carter is approved, and it is acceptable in quality and

form for publication on microfilm and electronically:

_____

_____

_____

_____

_____
                                                           Chair

University of California, San Diego

2011

DEDICATION

For:

My parents who taught me to learn (and how to learn),
My brother who gave me my love of worlds (especially our own),
My friends (who are great),
And the hope that insight and conscience can inform action.

TABLE OF CONTENTS

LIST OF ABBREVIATIONS

ΔC^*	—	An inverse technique used to estimate anthropogenic CO_2 content
AAIW	—	Antarctic Intermediate Water
ACC	—	Antarctic Circumpolar Current
CLIVAR	—	Climate Variability (Hydrographic program)
CFC	—	Chlorofluorocarbon
CTD	—	A conductivity, temperature, and pressure sensor
DML	—	Deep Mixed Layer
GLODAP	—	Global Data Analysis Project
LAN	—	Local Area Network
MLR	—	Multiple Linear Regression
OMP	—	Optimum Multiparameter (a type of inverse model)
P16S	—	The name of a section in the Southern Pacific
P18S	—	The name of a section in the Southern Pacific
PF	—	Polar Front
SACCF	—	Southern Antarctic Circumpolar Current Front
SAF	—	Subantarctic Front
SAM	—	Southern Annular Mode
SAMW	—	Subantarctic Mode Water
SSW	—	Subtropical Surface Water
STF	—	Subtropical Front
TA°	—	An estimate of preformed total alkalinity
TA*	—	A method for estimating calcium carbonate dissolution rates
UCDW	—	Upper Circumpolar Deep Water

LIST OF SYMBOLS

General

γ^n	—	Neutral density
σ_Θ	—	Potential density
Θ	—	Potential temperature
A_T	—	Total alkalinity
C_{org}	—	Total dissolved inorganic carbon exchanged via soft tissue pump
C_T	—	Total dissolved inorganic carbon
h	—	Total dissolved inorganic carbon exchanged via hard tissue pump
N (subscript)	—	Nitrate
$p(X)$	—	Partial pressure of gas "X"
r_H	—	Rate of the hard tissue pump
r_S	—	Rate of the soft tissue pump
$R_{X:Y}$	—	Redfield ratio between species "X" and "Y"
S	—	Salinity
s	—	Total phosphate exchanged via soft tissue pump
Si (subscript)	—	Total silicate

Chapter 1 specific

ε_λ	—	Extinction coefficient at wavelength λ
A'	—	Absorbance for sample with normal dye amount
A''	—	Absorbance ratio for sample with twice the normal dye amount
A_λ	—	Baseline adjusted absorbance at wavelength λ
A_λ°	—	Measured absorbance at wavelength λ
B_λ	—	Baseline absorbance at wavelength λ
e	—	Fraction of DML layer gas saturation
$[H^+]$	—	Proton concentration expressed on the total hydrogen ion scale
$[H^+]_{Free}$	—	Proton concentration expressed on the free hydrogen ion scale
HI^-	—	Singly protonated indicator dye species
I^{2-}	—	Fully deprotonated indicator dye species
l	—	Cell path-length
R' or R	—	Absorbance ratio for sample with normal dye amount
R''	—	Absorbance ratio for sample with twice the normal dye amount

Chapter 2 specific

Θ_x	—	Potential temperature of component X
a	—	Ventilation age
e	—	An extinction coefficient ratio
f_x	—	Fraction of component x composing a mixture
S_x	—	Salinity of component X
X'	—	Mixing-only value of property X
X''	—	Mixing-only value of property X after accounting for gas-exchange

Chapter 3 specific

Δbio	—	Change in biological "age"
Δf	—	Change in freshwater budget
ΔgC	—	Change in total dissolved inorganic carbon gas exchange budget
ΔgO	—	Change in oxygen gas exchange budget
Δh	—	Change in heat budget
Δz	—	Change in water density from vertical displacements
e	—	Vector of model–data residuals
D	—	Data matrix
M	—	Model output matrix used to scale the process matrix
P	—	Process matrix composed of process vectors
X_W	—	Matrix X after being weighted

LIST OF FIGURES

LIST OF TABLES

ACKNOWLDGEMENTS

Research Topics
• Analytical seawater carbonate system chemistry.
• Inverse modeling of biogeochemical processes in the ocean.

Education
2004   Bachelor of Arts in Earth and Planetary Sciences and Bachelor of Science in Chemistry, University of California at Berkeley, High Honors
2007   Modeling workshop, IFM-GEOMAR in Kiel Germany
2011   Doctor of Philosophy in Chemical Oceanography, Scripps Institution of Oceanography

Cruise Experience		– Total ship time: 148 days
CLIVAR I5	(2009)	– Seawater pH analyst
CLIVAR I6	(2008)	– Seawater pH analyst
AAIW05	(2005)	– A_T and C_T analyst

Conferences

Ocean Sciences 2010	Poster – "Potential alkalinity as a tracer for near-surface mixing: estimating gas exchange near the Polar Front."
GRC Mar. Chem. 2009	Poster – "An automated spectrophotometric pH system for at-sea measurements."
Ocean Sciences 2006	Poster – "A preliminary look at the AAIW05 dataset."

Publications in preparation
• Carter, B.R., Radich, J.A., Dickson A.G., An automated spectrophotometric system for discrete and underway seawater pH measurements. *Limnology and Oceanography: Methods.* Submitted Nov-2010.
• Carter, B.R., Dickson, A.G., A model for biogeochemical cycling in deep mixed layer waters entrained into Subantarctic Mode and Antarctic Intermediate Waters. *Global Biogeochemical Cycles*. Expected submission Mar-2011.
• Carter, B.R., Dickson A.G., Inferring changes in biogeochemical processes from hydrographic property measurements in the Pacific sector of the Southern Ocean. In prep for *Global Biogeochemical Cycles*. Expected submission May-2011.

Fellowships and elected offices
• Achievement Rewards for College Scientists Fellowship (2006-2010)
• UCSD Graduate Student Association: Elected VP of Finances (2008-2009)
• Chancellor's Fellow: University of California at San Diego (2004-2008)

Teaching
• Teaching Assistant for Chem. 6 BL (spring 2005) and SIO 141/Chem. 174 (spring 2010).
• Private Tutor in math and science (Jan-2007 to May-2008).

ABSTRACT OF THE DISSERTATION

Methods for Hydrographic Data Collection and Use
Applied to Infer Biogeochemistry in the Southern Ocean

by

Brendan Rae Carter

Doctor of Philosophy in Oceanography

University of California, San Diego, 2011

Professor Andrew Dickson, Chair

Data-based estimates of marine biogeochemical cycling are essential for making

accurate forecasts of changes to our planet's climate and ecosystems resulting from

mankind's perturbations to the chemistry of the ocean and the atmosphere. In this thesis I

present and apply novel methods for hydrographic data collection and analysis.

The quality and coverage of hydrographic measurements must be balanced

against the practical costs of the analyses. A system for efficient, semi-autonomous, and

precise colorimetric seawater pH analyses is presented and assessed with the aim of

decreasing the investment required for this measurement.

An inverse model constructed to estimate rates of organic matter degradation,

rates of calcium carbonate dissolution, measurement covariance resulting from organic

matter degradation, and the length of time that a measured water parcel has been out of

contact with the atmosphere is presented and applied in the Southern Ocean. Model

estimates are compared to estimates obtained from similar inverse methods that neglect

either diapycnal mixing or mixing altogether, and significant differences are found. This supports the findings of several recent research efforts warning against over-interpreting inverse methods that neglect mixing.

Climate models and ocean and atmospheric monitoring suggest that the Southern Ocean is undergoing long-term changes in its freshwater budget, heat budget, gas exchange processes, and circulation patterns. I examine and model the effects of changes in biogeochemical processes on hydrographic properties using differences between datasets collected more than a decade apart in the Pacific sector of the Southern Ocean. Results indicate a continuation of previously observed warming and freshening trends in intermediate and mode waters and evidence for an increase in the Ekman divergence driven upwelling in the Antarctic Circumpolar Current.

Introduction

Analytical advances of the 20th century have revealed that humans have significantly changed the chemical composition of the atmosphere and the over the last 200 years. The ocean is the planet's largest reservoir for carbon dioxide – a chemical released by mankind's activities with a dominant role in the Earth's climate and ocean chemistry. The amount of carbon dioxide in the oceans is almost 40 times that in the atmosphere. The ocean is therefore likely to eventually absorb the majority of this chemical released by humanity. This is a mixed blessing: carbon in the oceans does not perturb the Earth's radiation balance, but it reacts with water to form a weak acid. The influx of this chemical has resulted in measurable acidification of the surface ocean, and research has shown that ocean pH affects the viability of many ecologically important organisms [*Doney et al.*, 2009]. Additionally, the ocean's ability to sequester carbon dioxide from the atmosphere decreases as the pH of the ocean decreases. It is increasingly clear that predictions regarding the future of the Earth's oceans and climate depend upon an understanding of the processes governing the uptake of carbon dioxide and similar chemicals from the atmosphere into the ocean.

Increased recognition of the importance of biogeochemical cycling has spawned a global effort to document the state of the ocean's chemistry as it evolves in response to natural and anthropogenic (man-made) perturbations. I have been fortunate enough to be involved in the analytical and data interpretation arms of this program, and this document contains a summary of my work to date associated with these efforts.

This study— My aim has been to characterize processes controlling chemical cycling in the ocean and how these processes have changed in recent years. The chapters of this thesis can be thought of as a house of cards, each level built upon the last, with the view being furthest from the top. The first chapter is one answer (of many) to the question of "how can we observe the ocean?" The second deals with "what patterns do we see in these observations of the ocean, and how might these relate to biogeochemical processes?" The last chapter asks "what do these observations tell us about how these processes are changing over time?" In this sense, my focus becomes increasingly broad as it shifts from observations, to patterns in observations, to changes in the observed patterns over time.

The first chapter—My first concern is how best (from a practical standpoint) to observe the chemicals being released by mankind as they accumulate in the ocean and perturb its chemistry. Astute analytical chemists have explored the chemistry of carbon dioxide in seawater in great detail. While the reactions that carbon dioxide participates in in seawater are complex, the chemical concentrations of the various species involved can be estimated given values of the ionic strength of the seawater media, estimates of the concentrations of non carbon-containing alkaline species (silicate, phosphate, and borate), the physical properties (temperature and pressure), and at least two additional chemical measurements relevant to carbon dioxide in seawater [*Dickson et al.* 2007]. These additional chemical measurements are collectively referred to as carbonate system parameters. The majority of these required properties are measured routinely along hydrographic sections, though a choice must be made as to which of the carbonate system parameters will be measured. This decision is made in light of the balance between the

information gained against the practical costs of the analysis. Any hydrographic data collection effort therefore stands to benefit from improvements in the quality or decreases in the cost of these carbonate system measurements.

The four most straightforwardly-measured carbonate system parameters are: hydrogen ion concentration (expressed as pH), total dissolved inorganic carbon (C_T), total alkalinity (A_T), and the partial pressure or fugacity of CO_2 gas ($p(CO_2)$ or $f(CO_2)$). Typically, C_T and A_T are used when examining the carbonate system in seawater since they change in straightforward ways in response to oceanographic processes and do not change with pressure or temperature. However, seawater pH, which is related to the A_T to C_T ratio at a constant temperature and pressure, can often be measured faster and with greater repeatability than the other parameters. These advantages make pH an ideal option for characterizing the carbonate system for many applications, including, possibly, examination of small long-term changes in the state of the carbonate system. Even when two other measurements are already available, there is sufficient uncertainty in each of the measurements and equilibrium constant sets that information is gained by over-determining the system [*Lee et al.*, 1996; *McElligott et al.*, 1998; *Millero et al.*, 1993].

The first chapter of this work discusses attempts to automate the colorimetric seawater pH measurement technique. The automation of this method simplifies the procedure, decreases the amount of operator time required for each analysis, and demonstrates that the technique's high precision can be obtained using straightforward hydrographic sample collection practices. This chapter also assesses and discusses the sources of uncertainty for this measurement. While the measurement repeatability is excellent, the measurement accuracy has several limitations; most notably the absence of

a well-established seawater pH reference material. Accuracy uncertainties in these measurements are attributable to numerous causes, but we show that the majority is associated with likely impurities in the indicator dyes employed. Until this issue is resolved, it is clear that observations of long-term pH changes should be made using a single dye source so that measurements can be compared. The refined and automated colorimetric pH analysis technique developed in this chapter has been employed to contribute pH data for three hydrographic cruises (and a fourth as this is being written).

The underdetermined ocean—Once hydrographic records have been collected, the next challenge is how to infer the activity of processes in the ocean from these records. The central challenge is that multiple processes typically control the concentration of any single chemical species. For example, concentrations of the total dissolved inorganic carbon in the ocean can be changed by gas exchange with the atmosphere, uptake during photosynthesis, release during the degradation of organic matter, uptake to form calcium carbonate, release during calcium carbonate dissolution, dilution with freshwater, or mixing with another water mass with a different concentration. For each property measured there are therefore several additional processes that must be solved for. Thinking of processes as unknowns and properties as constraints, this then begins as the classic unsolvable algebra problem.

There are several strategies for reducing the number of unknowns. A key strategy is to exploit patterns of covariance in the ocean. For example, the Redfield ratio is an empirically-derived concept that relates the relative quantities of various chemicals that are removed or released through the formation or degradation of organic matter [*Redfield et al.*, 1963]. The optimal values of this ratio are contested [*Anderson and Sarmiento*,

1994; *Kortzinger et al.*, 2001; *Li and Peng*, 2003; *Takahashi et al.*, 1985], but the concept

is widely applied in chemical oceanography. The assumptions inherent to this concept

allow terms for biological changes in several chemical concentrations to be collapsed to a

single term. Another example of covariance between properties resulting from a process

is freshwater dilution, which acts to bring all concentrations closer to the freshwater's

chemical concentrations. A second common strategy is to make informed guesses as to

which processes will have essentially negligible effects on the measured chemical

concentrations. These processes are then neglected, though often considered as potential

sources of error for other process estimates. Unknowns are often eliminated via these

techniques until the problem becomes determined or over-determined.

Neglecting mixing— Mixing in the ocean is one such process that is often

neglected to some degree. For instance, the TA* estimate of calcium carbonate

dissolution rates and the CFC approach to estimating how recently a water mass has been

ventilated both neglect mixing entirely [*Sabine et al.*, 2004; *Sonnerup et al.*, 2001]. Also,

the most commonly employed values for the Redfield ratio were obtained using the

assumption that diapycnal mixing (or mixing across density gradients) is essentially

negligible. Recent research has shown that these assumptions are likely to lead to

substantial biases on a regional basis for all three of these approaches [*Friis et al.*, 2006;

Li and Peng, 2003; *Mecking et al.*, 2004].

The bias introduced by neglecting diapycnal mixing is likely to be especially large

for regions where the curvature of the distribution of the property of interest with respect

to depth is high and where stratification is low. Subantarctic Mode Water (SAMW) and

Antarctic Intermediate Water (AAIW) are related water masses with local minima in

stratification [*Sloyan et al.*, 2010] and local extrema in several properties. These water masses are thought to form largely from the incorporation of water from deep wintertime mixed layers found in the southeastern Pacific sector of the Southern Ocean [*Sloyan and Rintoul*, 2000]. They are responsible for the ventilation of the majority of the world's thermoclines and are thought to be responsible for a significant fraction of the ocean's anthropogenic carbon dioxide uptake [*Sabine et al.*, 2004].

The second chapter— In the second chapter, I estimate several biogeochemical processes both with and without neglecting mixing to see how sensitive the results are to this assumption. To do this, I take advantage of a novel hydrographic cruise conducted in the region and season of SAMW and AAIW formation. Direct measurements of the deep wintertime mixed layers at the surface of the ocean provide an estimate of the initial properties of this entrained water. This analysis allows for diapycnal mixing with both a deeper (denser) and a more northerly (less dense) water mass.

Assessing changes in the Southern Ocean— The water masses formed in the Southern Ocean are of special interest because this region is a hotspot of global climate change. Observations and global circulation models indicate long term changes in heat budgets, freshwater budgets, circulation patterns, and gas exchange patterns in this region [*Aoki et al.*, 2005; *Böning et al.*, 2008; *LeQuéré et al.*, 2007; *Lovenduski et al.*, 2007, 2008; *Thompson and Solomon*, 2002; *Gnanadesikan et al.*, 2007]. However, quantifying these trends from hydrographic sections has proven difficult for lack of an appropriate coordinate system with which to compare changes. Comparing changes along depth surfaces is complicated by the potential for vertical shifts in the location of water masses. In the vertically stratified ocean, these can lead to large apparent changes in temperature

or salinity in the absence of any change in heat or freshwater content. Surfaces of constant density are themselves defined by the temperature and the salinity, so heat or freshwater exchange can lead to a similar comparison between two different water masses. A typical approach to this problem is to use datasets collected over a range of times in order to average out any vertical shifts along surfaces of constant depth. However, the sampling pattern of the recent global hydrographic effort allows for a single visitation of a region once every 10-15 years, so this option is not always available.

The third chapter— In the third chapter, I assess long term trends in the water masses of the Southern Ocean using pairs of hydrographic records in the Southern Pacific. I also develop an inverse optimum multiparameter model to allow estimation of the magnitude of these trends from these dataset pairs. A key feature of this model is the use of changes in chemical measurements that are not typically considered in this type of comparison to estimate the influence of vertical shifts between the two records. This allows for estimation of the changes such shifts may have introduced into the property measurements that *are* typically considered as well as exploration of patterns in the vertical shifts themselves.

This thesis contributes to the global hydrographic data collection and interpretation effort in several ways. It presents a method for rapid and straightforward colorimetric seawater pH analysis with excellent analytical precision for hydrographic samples. It examines the biogeochemical cycling in the surface of the Pacific sector of the Southern Ocean and estimates rates of organic matter degradation and calcium carbonate dissolution for this region. It estimates the sensitivity of inverse methods to the bias inherent on neglecting mixing to various degrees, and suggests that a commonly

employed method for estimation of shallow water calcium carbonate dissolution may routinely overestimate this term. This, in turn, has implications for estimates of global calcium carbonate cycling. This sensitivity analysis also provides additional evidence to suggest that the most commonly used Redfield ratios, central assumptions for many methods for estimating processes from oceanographic data, may have large uncertainties as a result of not accounting for diapycnal mixing. Additionally, a novel method for CFC ventilation date estimation is presented that qualitatively matches the expected age distribution in the surface ocean despite the well-established biasing effects of subsurface mixing. A novel inverse model for estimating long-term trends from dataset pairs is presented and assessed. This model is utilized to confirm a continuation of trends found using comparisons between earlier hydrographic records and predicted using circulation models.

References for Introduction

Anderson, L. A. and J. L. Sarmiento (1994), Redfield ratios of remineralization determined by nutrient data analysis, *Global Biogeochem. Cycles, 8*, 65-80.

Aoki, S., N. L. Bindoff, and J. A. Church (2005), Interdecadal water mass changes in the Southern Ocean between 30 E and 160 E, *Geophys. Res. Lett., 32*, L07607.

Banks, H. T. and N. L. Bindoff (2003), Comparison of Observed Temperature and Salinity Changes in the Indo-Pacific with Results from the Coupled Climate Model HadCM3: Processes and Mechanisms, *J. Clim., 16*, 156-166.

Böning, C. W., A. Dispert, M. Visbeck, S. R. Rintoul, and F. U. Schwarzkopf (2008), The response of the Antarctic Circumpolar Current to recent climate change, *Nature Geoscience, 1*, 864-869.

Dickson, A. G., C. L. Sabine, and J. R. Christian (2007), Guide to best practices for ocean CO_2 measurements.

Doney, S. C., V. J. Fabry, R. A. Feely, and J. A. Kleypas (2009), Ocean acidification: the other CO_2 problem, *Marine Science, 1*, 169-192.

Friis, K., R. G. Najjar, M. J. Follows, and S. Dutkiewicz (2006), Possible overestimation of shallow-depth calcium carbonate dissolution in the ocean, *Global Biogeochem. Cycles, 20*, GB4019.

Gnanadesikan, A., J. L. Russell, and F. Zeng (2007), How does ocean ventilation change under global warming?, *Ocean Science, 3*, 43-53.

Kortzinger, A., J. I. Hedges, and P. D. Quay (2001), Redfield ratios revisited: Removing the biasing effect of anthropogenic CO_2, *Limnol. Oceanogr.*, 964-970.

Le Quéré, C., C. Rodenbeck, E. T. Buitenhuis, T. J. Conway, R. Langenfelds, A. Gomez, C. Labuschagne, M. Ramonet, T. Nakazawa, and N. Metzl (2007), Saturation of the Southern Ocean CO_2 sink due to recent climate change, *Science, 316*, 1735.

Lee, K., F. J. Millero, and D. M. Campbell (1996), The reliability of the thermodynamic constants for the dissociation of carbonic acid in seawater, *Mar. Chem., 55*, 233-245.

Lovenduski, N. S., N. Gruber, and S. C. Doney (2008), Toward a mechanistic understanding of the decadal trends in the Southern Ocean carbon sink, *Global Biogeochem. Cycles, 22*, GB3016.

Lovenduski, N. S., N. Gruber, S. C. Doney, and I. D. Lima (2007), Enhanced CO_2 outgassing in the Southern Ocean from a positive phase of the Southern Annular Mode, *Global Biogeochem. Cycles, 21*, GB2026.

McElligott, S., R. H. Byrne, K. Lee, R. Wanninkhof, F. J. Millero, and R. A. Feely (1998), Discrete water column measurements of CO_2 fugacity and pHT in seawater: A comparison of direct measurements and thermodynamic calculations, *Mar. Chem., 60*, 63-73.

Mecking, S., M. J. Warner, C. E. Greene, S. L. Hautala, and R. E. Sonnerup (2004), Influence of mixing on CFC uptake and CFC ages in the North Pacific thermocline, C07014.

Millero, F. J., R. H. Byrne, R. Wanninkhof, R. Feely, T. Clayton, P. Murphy, and M. F. Lamb (1993), The internal consistency of CO_2 measurements in the equatorial Pacific, *Mar. Chem., 44*, 269-280.

Redfield, A. C., B. H. Ketchum, and F. A. Richards (1963), The influence of organisms on the composition of sea-water, 26-77.

Sabine, C. L., R. A. Feely, N. Gruber, R. M. Key, K. Lee, J. L. Bullister, R. Wanninkhof, C. S. Wong, D. W. R. Wallace, and B. Tilbrook (2004), The oceanic sink for anthropogenic CO_2, *Science, 305*, 367-371.

Sloyan, B. M. and S. R. Rintoul (2001), The Southern Ocean Limb of the Global Deep Overturning Circulation, 143-173.

Sloyan, B. M., L. D. Talley, T. K. Chereskin, R. Fine, and J. Holte (2010), Antarctic Intermediate Water and Subantarctic Mode Water Formation in the southeast Pacific: the role of turbulent mixing, *J. Phys. Oceanogr.*, DOI: 10.1175/2010JPO4114.

Sonnerup, R. E. (2001), On the relations among CFC derived water mass ages, *Geophys. Res. Lett., 28*, 1739-1742.

Takahashi, T., W. S. Broecker, and S. Langer (1985), Redfield ratio based on chemical data from isopycnal surfaces, *Journal of Geophysical Research, 90*, 6907-6924.

Chapter 1: An automated system for spectrophotometric seawater pH measurements

1.1 Abstract

Spectrophotometric pH measurements stand to benefit greatly from the consistency and speed made possible through automation. Here we describe a simple, fast, and precise automated spectrophotometric pH measurement system for hydrographic samples. The system requires 4 minutes per analysis, 60 mL of sample, and little operator interaction, to obtain a repeatability comparable to the best results published with other techniques (±0.0004). The system and the suggested sample handling methods are assessed using over 5,000 at-sea measurements obtained during a hydrographic cruise in the Indian Ocean. Although the system is capable of high precision, our estimate of the likely accuracy of current spectrophotometric pH measurements is 0.01 to 0.02 pH units. We provide our rationale for this estimate based on assessments of the likely uncertainty contributions. At this time, the largest uncertainty is due to a lack of confidence in the purity of commercially available dyes, and the implication of this for spectrophotometric pH measurements.

1.2 Introduction

There is a growing need for a procedure that enables pH measurements to be made straightforwardly and reliably on discrete samples of seawater. Large numbers of such samples will be collected in the course of ocean monitoring efforts aimed at describing the oceanic carbon dioxide system and quantifying changes in seawater

composition due to the addition of anthropogenic carbon dioxide. Similarly, we expect additional pH measurements will be made to help characterize the seawater composition in a variety of ocean acidification experiments that study the response of organisms to varying seawater carbon dioxide levels [*National Research Council*, 2010].

Although the use of colorimetric indicator dyes for seawater pH determination was first used in the early 20th century [*Sørensen & Palitzsch*, 1910; *McClendon*, 1917], it was not until much later that Byrne and his co-workers [*Roberto-Baldo et al.*, 1985; *Byrne*,1987; *Byrne and Breland*, 1989] showed that spectrophotometric techniques using such colorimetric indicator dyes could be used to determine the pH of seawater with high repeatability.

To date, most seawater pH measurements using indicator dyes have been based on manual measurement of discrete samples (see SOP 6b in *Dickson et al.* [2007] which is based on a procedure that was drafted by Tonya Clayton, implementing the measurements described in *Clayton and Byrne* [1993]). The apparent simplicity of such measurements has also led to a number of analytical systems that can measure pH automatically on a pumped stream of seawater using a spectrophotometric procedure [*Bellerby et al.*, 1995, 2002; *Dickson*, 1998; *Tapp et al.*, 2000].

Here we describe an analytical system that can be used to implement the standard spectrophotometric approach for discrete samples in a semi-automated procedure. With this system it is practical to measure the pH of a series of discrete seawater samples in simple and straightforward fashion, each measurement taking about 4 minutes, while still enjoying the high reproducibility that has become the hallmark of such measurements. Unfortunately, as we relate below, there are still a few questions as to the ultimate

uncertainty of spectrophotometric pH measurements. Nevertheless, we feel our technique can be valuable to others despite these reservations, and are confident it will be yet more valuable once such problems have been resolved.

Throughout this paper we refer to pH as defined by the following expression:

$$pH = -\lg\left(\frac{[H^+]}{\text{mol kg}^{-1}}\right) \tag{1}$$

where the hydrogen ion concentration (in moles per kilogram of seawater) is expressed as the *total* hydrogen ion concentration, i.e. including the complexes of hydrogen ion with both water molecules and with sulfate ions [*Dickson*, 1993]:

$$[H^+] = [H^+_{\text{Free}}]\left(1 + S_T/K_S\right) \approx [H^+_{\text{Free}}] + [HSO_4^-] \tag{2}$$

Here, $[H^+_{\text{Free}}]$ is the concentration of *free* hydrogen ions (including complexes with water molecules), S_T is the total amount of sulfate ion in the seawater (a function of the salinity), and K_S is the acid dissociation constant for the hydrogen sulfate ion (at the appropriate salinity, temperature, and pressure).

In the spectrophotometric approach to measuring seawater pH, a pH indicator dye (usually a sulfonephthalein compound) is added to the seawater. Such dyes, although diprotic, behave in seawater essentially as monoprotic acids. The acid and base forms have distinct absorption spectra in the visible region, resulting in an unambiguous color change as the solution pH changes. The distinct spectra allow the relative concentration of the acid and base forms of the dye in the solution to be estimated spectrophotometrically (provided the appropriate extinction coefficient information is

known). The pH can then be estimated from the logarithmic form of the equilibrium equation:

$$pH = -\lg K(HI^-) + \lg\left(\frac{[I^{2-}]}{[HI^-]}\right) \tag{3}$$

In (3) the acid dissociation constant, $K(HI^-)$ of the singly-protonated form of the dye is a function of salinity, temperature, and pressure (as are the extinction coefficients).

As spectrophotometers are capable of measuring absorbance ratios with a high degree of reproducibility, the concentration in (3) can be estimated with excellent precision provided care is taken to estimate the appropriate spectrophotometric background and to control the measurement temperature. Our automated system for sample handling addresses these concerns while also avoiding prolonged exposure of the samples to the atmosphere.

1.3 Materials and Procedures

Theory and Calculations— We used the water soluble sodium salt of meta-cresol purple [*m*-cresol; Acros Organics lot no: A014923001] for the work reported here, as did *Clayton and Byrne* [1993] who used material obtained from Kodak. The approach we use can, of course, be used with other dyes. Similarly, our approach to data treatment parallels that of *Clayton and Byrne* [1993], though with some minor modifications appropriate to our particular measurement system.

The absorption spectrum of *m*-cresol purple in the seawater pH range is dominated by the absorption due to two species: the fully deprotonated form of the dye, I^{2-}, which appears purple to the human eye and has a maximum absorbance at a wavelength of 578 nm, and the partially deprotonated form, HI^-, which appears yellow to

the human eye and has a maximum absorbance at 434 nm. The fully protonated form, H_2I, is essentially absent in the open-ocean pH range.

In a seawater sample (containing the HI^- and I^{2-} forms of the dye), the absorbance at a particular wavelength, λ, normalized for the cell-length, l, is given in accordance with the Beer-Lambert law by the expression:

$$\frac{A_\lambda}{l} = \varepsilon_\lambda(HI^-) \cdot [HI^-] + \varepsilon_\lambda(I^{2-}) \cdot [I^{2-}] + B_\lambda + e \qquad (4)$$

where $\varepsilon_\lambda(HI^-)$ and $\varepsilon_\lambda(I^{2-})$ are the extinction coefficients of the specified forms of the dye at that wavelength, B_λ is the background absorption due to other species in the solution, and e is an error term due to instrumental noise. In the case that two wavelengths are used, and provided the background and non-random error terms can be removed by an appropriate subtractive procedure (see below) then equation (4) can be rearranged to give:

$$\frac{[I^{2-}]}{[HI^-]} = \frac{A_1/A_2 - \varepsilon_1(HI^-)/\varepsilon_2(HI^-)}{\varepsilon_1(I^{2-})/\varepsilon_2(HI^-) - (A_1/A_2)\varepsilon_2(I^{2-})/\varepsilon_2(HI^-)} \qquad (5)$$

where the subscripts 1 and 2 distinguish the wavelengths chosen. For the best sensitivity, the wavelengths used correspond to those of the absorbance maxima [*Byrne*, 1987]: 434 and 578 nm in the case of *m*-cresol purple. This expression can, in turn, be used together with equation (3) to infer the solution pH provided that $K(HI^-)$ and the three extinction coefficient ratios are known at the appropriate salinity and temperature (at 1 atm pressure). In this paper we have employed the data of *Clayton and Byrne* [1993] for these parameters – though with reservations noted below.

Modifications appropriate to use of a single-beam spectrophotometer— In their

numerous published papers, Byrne and his co-workers have consistently used a scanning

double beam spectrophotometer for their measurements of seawater pH. Nevertheless,

we decided instead to use a simpler and more robust diode array system (Agilent 8453).

A consequence of this choice is that changes in the intensity of the light source may occur

between the time when the background absorbance (that of the seawater solution without

dye) is measured and the time when the seawater and dye mixture's absorbance is

measured.

It thus becomes even more important to use the strategy suggested by *Byrne and

Breland* [1989] of also adjusting for changes in absorbance at wavelengths around

730 nm, where the *m*-cresol purple indicator does not absorb. The approach we took is as

follows:

1. We assume that any change in the absorbance over time is approximately

    identical at all wavelengths of interest. This appears to hold true to within about

    15%.

2. Rather than use a single wavelength (e.g.*,* 730 nm – Dickson et al. 2007) for this

    adjustment, we chose to average the results for the wavelength region between

    725 and 735 nm.

3. The adjustment was estimated and applied as follows:

$$A_\lambda = A_\lambda^0 - \sum_{n=725}^{n=735} A_n^0 / 11 \tag{6}$$

    where A_λ is the baseline adjusted absorbance at a wavelength λ and A_λ^0 is the

    original unadjusted absorbance at that wavelength returned by the

spectrophotometer from measurements on the background sample and on the sample with dye in it.

This approach averages out random fluctuations from diode to diode in the range from 725 to 735 nm, while adjusting for changes that are correlated over this wavelength range.

Correction for the pH change inherent on adding indicator dye to seawater— An indicator dye is itself an acid-base system that can change the pH of the seawater to which it is added. Since the pH of interest is that of the original unadulterated seawater, it is important to estimate and correct for this perturbation to the sample's pH. Here we emulate *Clayton and Byrne* [1993] in treating this perturbation as though it modified the measured absorbance ratio, A_{578} / A_{434}.

As the amount of dye added to our samples is somewhat variable (a consequence of using the same 25 mL syringe pump to meter both sample and dye) our approach differs somewhat from that described by *Clayton and Byrne* [1993]. We use the (adjusted) absorbance measured at the isosbestic wavelength, A_{isos}, (here we used A_{488}: the wavelength corresponding best in our spectrometer to the isosbestic wavelength of 487.6 nm described by *Clayton and Byrne* [1993]) as a proxy for the amount of dye present.

We prepared 3 seawater solutions with approximate pHs of 7.6, 7.9, and 8.2 and measured the absorbance ratio for each of these solutions, first with the usual amount of dye solution (~0.05 mL) added to ~15 mL of seawater, and then with approximately double that amount (~0.1 mL). These measurements were repeated 4 times on each of

the seawater solutions (24 measurements in all). For each solution the change in

absorbance ratio due to the added dye was calculated using:

$$\frac{\Delta R}{\Delta A} = \frac{\overline{R''} - \overline{R'}}{\overline{A''_{isos}} - \overline{A'_{isos}}} \tag{7}$$

where the various terms are the mean values, and the primes refer either to the usual dye

quantity (single prime) or to double that amount (double prime). The $\Delta R/\Delta A$ values are

an approximately linear function of R_1, i.e. $\Delta R / \Delta A = aR_1 + b$, and thus it is practical to

use this information to adjust values of R_1 to estimate the value of the absorbance ratio

that would have been observed if the dye solution had not perturbed the pH:

$$R = R' - A'_{isos}\left(aR' + b\right) \tag{8}$$

Computing pH from adjusted absorbance ratio measurements— As noted above,

the pH of a seawater / dye mixture can be estimated from an equation of the form

[*Clayton and Byrne*, 1993]:

$$pH = -\lg K(HI^-) + \lg\left(\frac{R - e_1}{e_2 - R \cdot e_3}\right) \tag{9}$$

In this equation R is the adjusted absorbance ratio, A_{578} / A_{434}, based on the adjusted

absorbances calculated using (6), with the ratio further adjusted for the effect of the dye

addition using (8), and e_1, e_2, and e_3 are the various ratios of extinction coefficients:

$$e_1 = \varepsilon_{578}(HI^-)\big/\varepsilon_{434}(HI^-) ; \quad e_2 = \varepsilon_{578}(I^{2-})\big/\varepsilon_{434}(HI^-) ; \quad e_3 = \varepsilon_{434}(I^{2-})\big/\varepsilon_{434}(HI^-) \tag{10}$$

The values for $-\lg K(\text{HI}^-)$ as a function of salinity and temperature, as well as values for e_1, e_2, and e_3 have been published by *Clayton and Byrne* [1993], who write (9) as:

$$\text{pH} = 1245.9 / T + (2.11 \times 10^{-3})(35 - S) + \lg\left(\frac{R - 0.00691}{2.2220 - R \cdot 0.1331} \right) \qquad (11)$$

where $293 \leq T \leq 303$ and $30 \leq S \leq 37$. This is the expression we use in this paper to calculate pH values for measurements we made at 20 °C.

The measurement system— A diagram of the seawater handling system is shown in Figure 1.1. The various components used are detailed in the figure legend. The temperature of the cell is controlled using water pumped from a Thermo Scientific Neslab RTE-7D refrigerated recirculating bath; a second such bath is used to bring samples to the desired temperature before analysis.

The absorbance measurements are made using an Agilent 8453 diode array spectrophotometer with a custom holder able to hold a 10 cm cylindrical cell rigidly in place. The spectrophotometer is tilted so that the cell is inclined 20° from the horizontal (with the outlet raised) to prevent bubble accumulation within the light path. For at-sea measurements the cell is oriented parallel to the axis of the ship that is the least prone to rotation (typically bow to stern).

The automation and data processing are controlled from a computer program written in LabVIEW (version 8.2). The Kloehn syringe pump and the YSI thermometer communicate with this program via serial RS-232 interfaces and the Agilent spectrophotometer uses TCP/IP over a LAN connection (with a crossover cable).

(A) Sample Introduction Tube

Optional
Rinse Water

To Thermostat
Bath

Port No.
1   2

**(E) Temperature
Pre-Equilibrator**

Outflow
to Waste

4   3

**(B) Sample
Bottle**

From Thermostat
Bath

(C) Dye Syringe

20.00 °C

(F) Spectrophotometer cell

(D) Automated Syringe Pump

(G) Thermometer
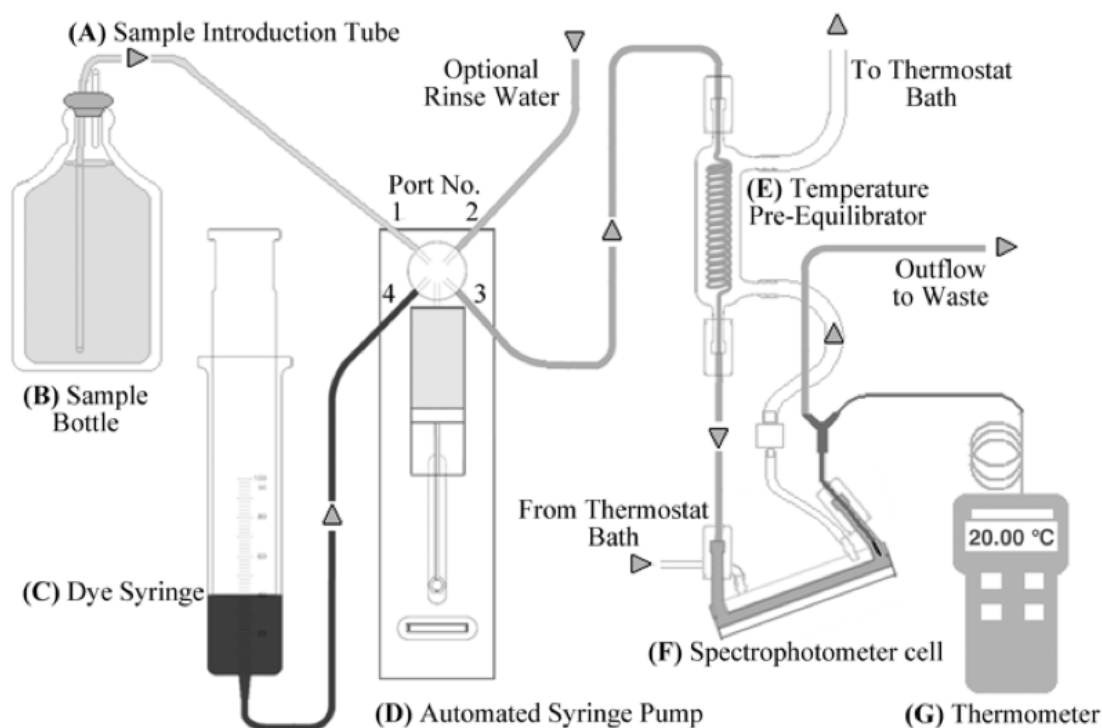
Figure 1.1 Schematic of automated measurement system. Arrows indicate the direction of flow through tubing (for the sample path we used Upchurch Scientific FEP 1/8" OD by 1/16" ID with connector nuts and ferrules). The system consists of the following components: (A) a sample introduction tube threaded through a flanged 2-leg grey butyl rubber stopper pierced by an additional (3 cm) length of tubing as a vent; (B) a custom 250 mL Schott DURAN® borosilicate glass serum sample bottle; (C) a Tomopal 100 mL glass syringe with dye (wrapped in aluminum foil to prevent UV exposure of the dye); (D) a Kloehn V6 automated syringe pump with a 25 mL syringe and a 4-port selector valve; (E) a Graham-style spiral condenser used as a temperature pre-equilibrator; (F) a custom, 10 cm, cylindrical, jacketed, flow-through, spectrophotometric cell (0.5 cm diameter sample tube) made from SUPRASIL® by Hellma Analytics; and (G) a YSI 4600 thermometer with a YSI 451 probe inserted through a Y junction into the downstream exit from the cell.

Setting up the measurement system for use— The system was assembled as

indicated in Figure 1.1, with the sample bottle (B) held in a home-made cup-holder

located directly above the syringe pump (D), the dye syringe (C) held by a laboratory

clamp to the side of the syringe pump, and the temperature pre-equilibrator (E) held by a

second laboratory clamp over the cell. The dye syringe was mounted so that the

syringe's outlet was approximately level with the valve at the top of the syringe pump (see discussion below).

The Agilent 8453 spectrophotometer was used with both tungsten and deuterium lamps operating together so as to improve the repeatability of the Agilent's absorbance measurements at the wavelength of maximum absorbance of the HI^- dye species (434 nm). Although *m*-cresol dye does degrade in the UV light from a deuterium lamp, we feel that this does not significantly affect our pH measurements.

Prior to analyses, the syringe pump is operated so as to ensure that the tubing, syringe (on the pump), and cell are filled with seawater. The system is then run through the analysis cycle at least once to confirm that dye is being delivered appropriately, and that spectra are being recorded.

Although the system can be left between analyses for a number of hours, if it was to be left for over 12 hours, we chose to flush the seawater path – including the syringe pump – with deionized water before leaving it. The dye solution itself was replaced about every 7–10 days. When cleaning the system thoroughly, the components were flushed with deionized water and disassembled to dry. The cell can be cleaned effectively by leaving 50% aqua regia (1 part HNO_3, 3 parts HCl, 4 parts water) in the cell overnight and then rinsing it thoroughly with deionized water. However, we have found that it is helpful to then soak the cell in seawater for at least 5 hours before use to reduce the tendency for bubbles to cling to the inside of the cell.

Dye preparation— As noted above, the dye we use is the sodium salt of *m*-cresol purple. To minimize the magnitude of any pH perturbation caused by adding the dye solution to seawater, it is desirable to match the dye pH to the pH of the samples to be

measured. Although this is not practical for samples over a range of pHs – such as in an oceanographic profile – we chose to adjust the dye pH to approximately 7.9, measured using an Orion SA210 portable pH meter calibrated on the NBS pH scale with pHydrion$^{®}$ pH buffers (pH 4.0 and pH 10.0).

Sample collection and measurement— Seawater pH is very sensitive to the gain or loss of CO_2 through gas exchange, and steps are taken to limit opportunities for exchange during sample collection, storage, and measurement. We deviated from the recommended sampling practices for C_T measurements [*Dickson et al.*, 2007] by avoiding headspace entirely when filling the sample container.

We use custom-made 250 mL serum bottles (13 mm neck ID) based on a Schott DURAN$^{®}$ glass blank to collect pH samples for analysis. The filling procedure is as follows:

(1) The bottle and stopper (flanged 2-leg plug, grey butyl rubber) are rinsed with the sample seawater three times, using ~ 50 mL of sample for each rinse.

(2) The bottle is filled from a flexible tube inserted to the bottom of the bottle, and the water is overflowed by approximately one bottle volume (judged by time). The tube is then removed while water is still flowing so as to fill the bottle completely.

(3) Samples are poisoned immediately with mercury (II) chloride (equivalent to 0.02% by volume of a saturated solution) injected about 1 cm below the surface of the sample.

(4) The grey butyl stopper is then inserted into the bottle, taking care to avoid any headspace.

Samples are then stored for later analysis, preferably less than four hours so as to limit the opportunity for any gas-exchange. Prior to analysis, the samples are brought close to the desired analysis temperature (within 1 °C of 20 °C) in a second temperature bath dedicated to this purpose. The samples were cycled through this bath, each remaining there for ~16 minutes. Colder samples expand measurably on warming, thus it is necessary to monitor the sample stoppers for signs of lifting and ensure they are firmly pushed back into the neck of the bottle before there is any opportunity for direct gas-exchange with the surrounding atmosphere.

The analysis procedure is as follows:

(1) The outside of the sample introduction tube (B) is wiped dry of the previous sample.

(2) The stopper is removed from the next sample bottle; a small amount (~5 mL) of water is removed; the sample bottle is placed in the cup-holder above the syringe pump; and the sample introduction tube and its butyl stopper are inserted.

(3) The automated measurement sequence is then initiated as soon as the previous sample has been analyzed completely.

We chose to speed up sample throughput by exchanging samples after the final rinse water was taken into the syringe. However, we took care to minimize the time a sample was waiting on the instrument prior to initiating the analysis.

The Kloehn syringe pump and its associated rotary valve control all fluid-flow through the system. The automated analysis sequence (programmed in LabVIEW) is as follows (for detailed timing, volumes, etc. see Table 1.1):

Table 1.1 A table showing the sequence of actions taken by the spectrophotometer and the syringe pump during a sample analysis. Time intervals are approximate (±3 seconds).

Time Interval (m:ss)	Syringe pump activity	Syringe position (mL)	Port no. open	Cell / spectrophotometer activity
0:00–0:15	1a: *fill with sample*	0 → 15	1	
0:15–0:25	1b: *dispense*	15 → 0	3	
0:25–0:40	2a: *fill with sample*	0 → 15	1	
0:40–0:50	2b: *dispense*	15 → 0	3	
0:50–1:00	3a: *add sample*	0 → 5	1	Background temperature equilibration:
1:00–1:05	3b: *add dye*	5 → 5+	4	~80 s wait to allow
1:05–1:20	3c: *fill with sample*	5+ → 15	1	seawater in cell to reach
1:20–2:10		15	1	thermostated temperature
2:10–2:20		15	1	Background spectrum
2:20–2:30	3d: *dispense*	15 → 0	3	
2:30–2:45	4a: *fill with rinse*	0 → 15	1 or 2	Seawater / dye mixture
2:45–3:48		15	1	temperature equilibration
3:48–3:50		15	1	Mixture Spectrum
3:50–4:00	4b: *dispense*	15 → 0	3	

(1) replace previous sample with new sample, flushing sufficiently to ensure that the spectrophotometric cell is now filled with fresh sample;

(2) wait 80 s to allow the seawater in the cell to reach the thermostated temperature, and then measure the background (without dye added) spectrum;

(3) replace the seawater in the cell with the seawater and dye mixture, wait 80 s to allow this mixture to reach the thermostated temperature, and then measure its spectrum;

(4) flush the dye/seawater mixture out of the cell with additional sample or – if sample seawater is limited – water from a rinse water reservoir (see Figure 1.1).

The system archives the original spectra as well as the system temperature and appropriate sample identification information. These data are then used to calculate the R value – the adjusted absorbance ratio, A_{578} / A_{434}, based on the adjusted absorbances calculated using (6), with the ratio further adjusted for the effect of the dye addition using (8). If the correct salinity is already known, the final pH value is calculated; otherwise it is calculated at a later time.

1.4 Assessment

Data used for method assessment— Over 5000 measurements of pH were made on hydrographic samples using this system aboard the *RV Roger Revelle* on the Climate Variability (CLIVAR) I5 hydrographic survey (March through May of 2009). This expedition collected water from up to 36 depths at 195 hydrographic stations spanning the Indian Ocean at approximately 35º S latitude. The timing presented in Table 1.1 was used for this cruise. Seawater sampled for pH was usually also analyzed by other researchers for C_T, A_T, salinity, phosphate, nitrate, nitrite, silicate, dissolved oxygen, CFCs, and a handful of other parameters.

Effects of adding HgCl₂— The routine addition of mercury(II) chloride ($HgCl_2$) to seawater samples raises the question of whether this addition is lowering the sample pH as saturated $HgCl_2$ is a slightly acidic solution. This was assessed using replicate samples of 12 different seawaters (collected at different depths). The amount of $HgCl_2$ added amounted to 0, 1, 2, or 3 times the usual addition, and the samples were measured in random order. The pH was found to change on average by -0.00027 ± 0.00005 (d.f. = 38; unless otherwise noted, uncertainties are expressed as standard deviations throughout this paper) for each aliquot of $HgCl_2$ added. Data from samples with a low initial pH (<7.8) showed a slightly smaller decrease (-0.00023) during dilution relative to samples with a higher initial pH (-0.00029). Thus we concluded that any change due to this was negligible.

Effects of bottle headspace— The sample pH will change if CO_2 is gained or lost to a headspace while it is in its sample bottle. We designed a simple experiment to assess the likely importance of this. We collected 24 pairs of samples (10 from within 50 m of the sea surface; 14 from deeper – and hence with higher CO_2 levels). One of the pair of bottles was treated as described above (essentially no headspace), the other had a headspace deliberately introduced of between 1–2% of the bottle volume. These samples were then analyzed for pH.

The mean difference in pH for bottles collected from near-surface waters was statistically indistinguishable from zero, -0.00011 ± 0.00072 (d.f. = 10), whereas there was a discernable increase in pH for the deeper samples, -0.00098 ± 0.00066 (d.f. = 14). This observation is in keeping with what would be expected if CO_2 had been lost from the sample into the bottle headspace.
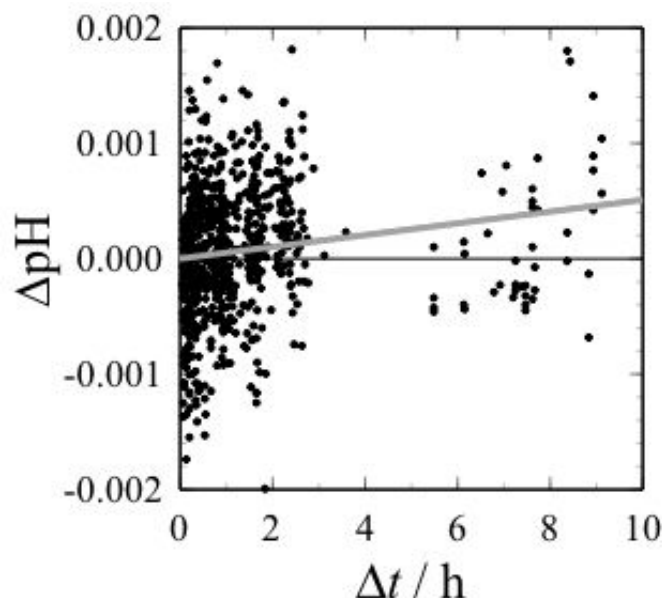
Figure 1.2 The apparent change in pH (20 °C) for replicate analyses plotted against the time (in hours) that had elapsed since the initial analysis.

Changes in seawater pH over time— As the pH measurement is potentially very sensitive, it is important that we have confidence that the sample collected is not changing significantly while awaiting analysis. We assessed the short-term stability of our samples using replicate samples as follows. Whenever duplicate samples were collected (~4 per profile), they were analyzed somewhat randomly during the course of analyzing samples from that particular profile (over the course of about 3 h); in a number of more limited cases a third replicate was collected and these were analyzed together with samples from the next profile (5–10 h after the original measurement). The changes in pH found are shown in Figure 1.2. These changes suggest that the pH of both the surface and the deep samples are increasing with time (~0.00005 pH units h^{-1}).

However, this magnitude of change has negligible influence on the pH measurements made on the cruise.

Measurement repeatability— The repeatability (as defined by *Taylor and Kuyatt*, [1994]) was assessed using pH measurements on samples collected in duplicate and analyzed within 3 h of each other. The standard deviation estimated from these measurements was 0.00042 pH units (d.f. = 657). This is comparable to the precision reported by *Clayton and Byrne* [1993].

Measurement reproducibility— Although reference materials for oceanic CO_2 measurements have not been certified for pH, their stability for total dissolved inorganic carbon and for total alkalinity suggests they could be used to assess longer-term reproducibility. On CLIVAR I5, we measured 6 bottles from Batch 93; the estimated standard deviation of these measurements was 0.0009 pH units. This reproducibility is comparable to other sets of pH measurements on similar reference materials. For example on a recent cruise (CLIVAR A13.5) we measured 16 bottles from Batch 98, and the estimated standard deviation was 0.0007 pH units. Nevertheless, there is a suggestion that a proportion of this variance could come from small systematic bottle-to-bottle differences in the reference material itself, and thus these numbers may represent an upper limit.
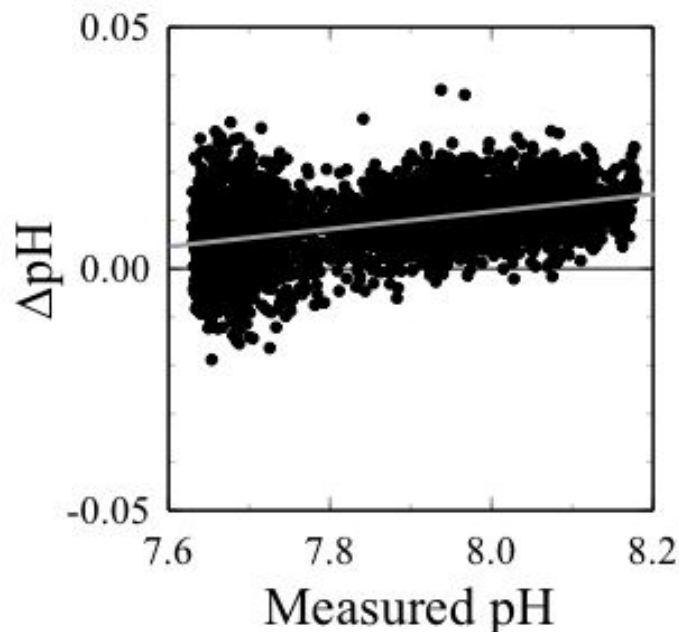
Figure 1.3 The difference: measured – estimated pH (at 20 °C), plotted against the measured pH (20 °C). Estimates of pH were obtained using carbonate system constants (Mehrbach et al. 1973 as refit by Dickson and Millero 1987) and measurements of A_T, C_T, silicate, phosphate, and salinity. All data used are preliminary measurements from a hydrographic cruise along CLIVAR leg I5; the line is the best fit.

Measurement accuracy— It is difficult to assess the accuracy of the method described since there are no seawater reference materials certified for pH and no inherently accurate alternate approaches to pH measurement. One approach is to assess the consistency of our pH values (measured at 20 °C) with pH values at 20 °C inferred from the measurements of total alkalinity and total dissolved inorganic carbon, together with measured values for salinity, total phosphate, and total silicate [*Pierrot et al.*, 2006; *Dickson et al.*, 2007]. The difference between the measured and calculated values is shown in Figure 1.3. If alternate published sets of carbonate system equilibrium constants had been used for this, the plot would appear of similar slope, but offset by

different amounts from the *x*-axis. The range of these offsets would be about 0.02–0.03 in pH! It is difficult to make a definitive statement as to the accuracy of our measurements from this, but it seems that a number in the range of 0.01–0.02 is plausible.
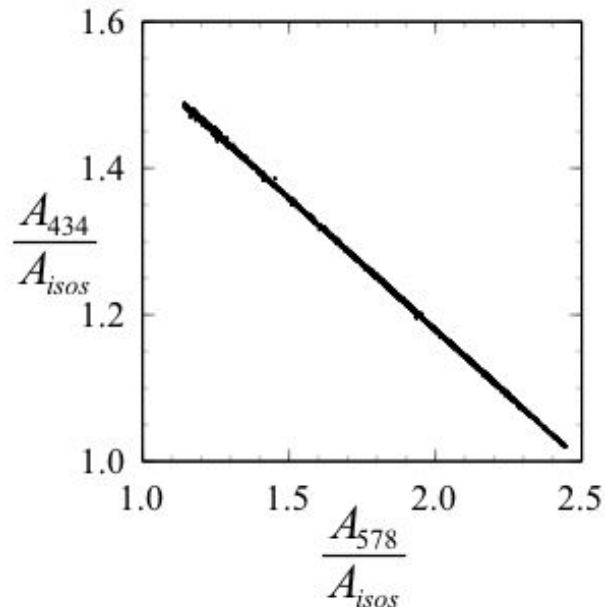
Figure 1.4 A plot of equation (12), i.e. A_{434}/A_{488} plotted against A_{578}/A_{488} (the peak absorbances normalized to the absorbance at the isosbestic wavelength). The plotted data are from CLIVAR leg I5.

A recent publication by *Yao et al.* [2007] suggests that the extinction coefficient ratios (10) published by *Clayton and Byrne* [1993], when used with dye obtained from a different manufacturer, may not give identical pH values. We thus sought to see if we could compare the extinction coefficient ratios implicit in our absorbance ratios with the published values. Although it is not practical to do this directly, a plot of A_{434}/A_{isos} against A_{578}/A_{isos} (the peak absorbances normalized to the absorbance at the isosbestic wavelength) has the form:

$$\frac{A_{434}}{A_{isos}} = \left(\frac{1-e_3}{e_1-e_2}\right)\left(\frac{A_{578}}{A_{isos}}\right) + b \tag{12}$$

 (Figure 1.4). Unfortunately, the slope estimated in Figure 1.4 (–0.358) is meaningfully different from the slope implied by the *Clayton and Byrne* [1993] data (–0.391). At this time, we do not have a sensible explanation for this difference but we assume it must reflect some difference in the extinction coefficient ratios in addition to any error inherent in treating absorbance measured at a single diode ($\lambda = 488$ nm) as a proxy for the absorbance at the isosbestic wavelength (487.6 nm, *Clayton and Byrne* [1993]).

1.5 Discussion

This approach to measuring seawater pH is both convenient and reproducible (when using the same batch of indicator dye – such as within a cruise). The samples are taken in a similar fashion to those for the other CO_2 parameters that depend on limiting the amount of gas exchange (i.e., $p(CO_2)$ on discrete samples; total dissolved inorganic carbon). They are then analyzed semi-automatically with the primary responsibility of the operator being to change one sample for the next. The precision is comparable to that reported for samples that are measured manually using a high-quality double-beam spectrophotometer [*Clayton and Byrne*, 1993; *Byrne et al.*, 2010]. Unfortunately, the overall uncertainty of the spectrophotometric method appears to be far worse than the precision – we estimate it to be between 0.01 and 0.02 pH units – and it is not well constrained.

The primary sources of uncertainty in our spectrophotometric pH measurements are likely to be in one or more of the following:

   a) the measurements of absorbance spectra;

   b) the measurements of salinity and temperature;

   c) the adjustment of the absorbance ratio to correct for the effects of dye addition;

d) the assumption that the dye is a pure chemical; and

e) the calibration of the properties of the indicator dye.

We discuss each of these in turn.

The spectrophotometer we use (Agilent 8453) is a high-quality diode-array system. We used National Institute of Standards and Technology (NIST) reference materials to confirm the wavelength accuracy. The absorbance accuracy is not well characterized (the instrument specifications state the maximum error as $< \pm 0.005$ absorbance units), but laboratory comparison of results between different instruments suggests that this is not a major uncertainty contribution. Furthermore, the strategy we use to adjust for changes in the light intensity between background and sample measurements improves the repeatability of our measurements.

The salinity is measured as part of the cruise data with an uncertainty of approximately ± 0.001. This has no perceptible effect on pH uncertainty. The temperature measurement was more problematic. In this system we tried to measure the temperature directly in the neck of the cell in the sample line (see Figure 1.1), this being as close to inside the cell as we could manage. Unfortunately, the probe we used was not sufficiently robust and it was not possible to be certain that the probe was appropriately immersed in the water we were measuring. We performed a number of calculations to assess the likely influence of temperature errors on pH measurement accuracy. Although the pH of the seawater being measured does depend significantly on temperature, the measured pH using an indicator dye does not [*Byrne and Breland*, 1989]. This is because the temperature dependence of the dye dissociation constant – see equation 10 – largely compensates for the temperature dependence of the various acid/base reactions occurring

in seawater that define the pH for a particular sample. Thus, even for a temperature error

as large as 1 °C, the resulting error in measured pH is always less than 0.001.

The magnitude of the pH change resulting from adjusting the absorbance ratio for

the addition of indicator dye was within ± 0.005 pH units. This is kept low by using a 10

cm cell, thus requiring less dye for a particular absorbance, and by adjusting the dye pH

to around 7.9 prior to use (as described above). The likely uncertainty due to this is

estimated to be < 0.002 in pH.

A recent paper by *Yao et al.* [2007] shows that there are clear indications of

impurities in *m*-cresol purple obtained from different manufacturers, and that dye from

these various manufacturers will give pH values on the same seawater sample that vary

over a range of about 0.01 pH units. Furthermore, the difference observed using dye

from two particular manufacturers (Kodak and Sigma Aldrich) varies between 0.001 at

pH 7.2 to 0.006 at pH 8.2. The exact reasons for this are not clear though it suggests the

likely existence of a pH-dependent colored impurity in the dye stock solutions used. At

this time Byrne and his group are endeavoring to purify this dye (personal

communication). Until that has been done, and the properties of a pure dye determined, it

is not possible to know the exact magnitude of this error component.

Throughout this paper we use the information for (Kodak) *m*-cresol purple

[*Clayton and Byrne*, 1993] even though we used dye obtained from Acros Organics. The

difference at a pH of about 8.1 noted by *Yao et al.* [2007] was about 0.002 in pH. The

dye equation (11) proposed by *Clayton and Byrne* [1993] has never been confirmed

independently. Indeed *Del Valls and Dickson* [1998] suggest that the value assumed for

the Tris buffer used in the original calibration could have been in error by about 0.005 pH

units. Nevertheless, at this time these are the only values available. It is therefore

necessary to consider how appropriate they are for our measurements. First, as noted

above, we did not use Kodak dye; second, we assume that the behavior of the Agilent

8453 spectrophotometer is essentially identical to that of the Cary Varian

spectrophotometers used by *Clayton and Byrne* [1993]; third, our measurements are made

at 20 °C, whereas the extinction coefficient ratios of Clayton and Byrne were measured at

25 °C. Some unpublished measurements from our laboratory suggest that a change of

spectrophotometers may result in a change in the measured pH of about 0.002 pH units.

In addition, an examination of the measurements of *Zhang and Byrne* [1996], who

measured the extinction coefficient ratios of the related thymol blue indicator over a

range of temperature, suggest that using data from 25 °C at 20 °C could result in an error

of up to 0.003 in pH.

The errors detailed above are dominated by the possible error resulting from

impurities in the dye (~0.01?). Thus we believe the overall uncertainty of our

spectrophotometric pH measurements resulting from the combination of all these errors

lies between 0.01 and 0.02 pH units. The data presented in Figure 1.3 do not provide any

reason to doubt this estimate.

The scatter in figure 1.3 is dominated by the random errors in the measurements

of total alkalinity and of total dissolved inorganic carbon underlying this figure. The

non-zero slope and offset of the line through the data imply that there are one or more

inconsistencies in the full suite of information used to calculate pH differences, i.e.,

systematic errors in the measured analytical parameters or in the equilibrium constants

used for the calculation. At this time it is not possible to assign cause.

1.6 Comments and Recommendations

As a result of our experience with this system we – in our own laboratory –
instituted some modifications to improve and / or simplify this system. We no longer use
the deuterium lamp in the Agilent 8453, measuring spectra using just the tungsten lamp.
To compensate for the added noise in our spectra, especially at 434 nm, we average 6
spectra measured rapidly one after another on the same solution in the cell. We have also
determined that the spiral temperature equilibrator is not needed when the sample
temperature is brought to within 1 °C of the desired temperature by immersion in a
thermostat bath, thus we have removed it from our system. In addition, we now estimate
the absorbance at the isosbestic wavelength (487.6 nm) as a weighted average of the
values at the two diodes 487 and 488 nm, rather than simply using the 488 nm value.

We have also decided to replace the YSI 451 probe placed directly in the sample
flow path with a more robust probe (YSI 406) placed in the recirculating thermostated
water just downstream of the cell. Although this may result in slightly more inaccurate
temperature measurements, we believe the gain in reliability will offset this, especially as
small temperature errors are not a significant problem for seawater measurements (see
discussion above).

As is seen from the discussion above, managing samples in such a way that there
is no headspace is awkward when using glass containers to contain the sample. This still
needs some improvement. Ideally, one would use a container that could change volume
as the sample warms and expands. The primary difficulty is that the only material that
has been shown to be well-suited to holding seawater samples for subsequent CO_2-related
measurements is Pyrex® or a borosilicate glass of a very similar composition

(unpublished results). We believe it is possible to limit the pH error associated with loss of CO_2 into the headspace of a glass bottle to less than 0.001 in pH by carefully controlling the volume of headspace to be no more than 1% of the total volume. We plan to do this in future by carefully removing a specified volume of water with an Eppendorf pipette.

Our present approach to arriving at a suitable estimate of the perturbation in pH (and hence R) caused by the addition of dye is unsatisfying. It is a simple empirical approach developed for open ocean seawaters that needs to be repeated for each new batch of dye solution, and ideally using seawater of similar composition to the seawater being measured. A paper by *Chierici et al.* [1999] uses an equilibrium approach to estimate likely dye perturbations, but this approach has not yet been applied to pH measurements. Clearly there is room for improvement in how this adjustment is applied.

The principal problem associated with spectrophotometric pH measurements at this time is not that they are awkward to make or of poor precision, but rather that the accuracy is not well constrained. This may, as *Yao et al.* [2007] suggest, be due solely to dye impurities; it remains to be seen. If and when pure dye becomes available and its properties characterized, the accuracy of spectrophotometric pH measurements will surely improve. Despite the problems with accuracy, it is possible – as has been shown by *Byrne et al.* [2010] – to detect small differences in pH with time such as those resulting from dissolution of anthropogenic CO_2 into ocean water provided that either the same dye lot is used throughout or appropriate adjustments made [*Yao et al.*, 2007].

1.7 Acknowledgements

References for Chapter 1

Bellerby, R. G. J., A. Olsen, T. Johannessen, and P. Croot (2002), A high precision spectrophotometric method for on-line shipboard seawater pH measurements: the automated marine pH sensor (AMpS)*, Talanta, 56*, 61-69.

Bellerby, R. G. J., D. R. Turner, G. E. Millward, and P. J. Worsfold (1995), Shipboard flow injection determination of sea water pH with spectrophotometric detection*, Anal. Chim. Acta, 309*, 259-270.

Byrne, R. H. (1987), Standardization of standard buffers by visible spectrometry*, Anal. Chem., 59*, 1479-1481.

Byrne, R. H. and J. A. Breland (1989), High precision multiwavelength pH determinations in seawater using cresol red*, Deep Sea Research Part A.Oceanographic Research Papers, 36*, 803-810.

Byrne, R. H., S. Mecking, R. A. Feely, and X. Liu (2010), Direct observations of basin-wide acidification of the North Pacific Ocean*, Geophys. Res. Lett., 37*, L02601.

Chierici, M., A. Fransson, and L. G. Anderson (1999), Influence of m-cresol purple indicator additions on the pH of seawater samples: correction factors evaluated from a chemical speciation model*, Mar. Chem., 65*, 281-290.

Clayton, T. D. and R. H. Byrne (1993), Spectrophotometric seawater pH measurements: total hydrogen ion concentration scale calibration of m-cresol purple and at-sea results*, Deep Sea Research Part I: Oceanographic Research Papers, 40*, 2115-2129.

DelValls, T. A. and A. G. Dickson (1998), The pH of buffers based on 2-amino-2-hydroxymethyl-1, 3-propanediol ('tris') in synthetic sea water*, Deep-Sea Research Part I, 45*, 1541-1554.

Dickson, A. G. (1993), The measurement of sea water pH*, Mar. Chem., 44*, 131-142.

Dickson, A. G. 1998. Underway measurement of pH: method and meaning. In *Proceedings of the Marc'hMor Workshop, IUEM Brest* (Ed. S. Blain), pp. 104–107.

Dickson, A. G. and F. J. Millero (1987), A comparison of the equilibrium constants for the dissociation of carbonic acid in seawater media*, Deep Sea Research Part A.Oceanographic Research Papers, 34*, 1733-1743.

Dickson, A. G., C. L. Sabine, and J. R. Christian (2007), Guide to best practices for ocean CO2 measurements.

McClendon, J. F. (1917), The standardization of a new colorimetric method for the determination of the hydrogen ion concentration, CO_2 tension, and CO_2 and O_2

content of sea water, of animal heat, and of CO_2 of the air, with a summary of similar data on bicarbonate solutions in general*, J. Biol. Chem., 30*, 265.

Mehrbach, C., C. H. Culberson, J. E. Hawley, and R. M. Pytkowicz (1973), Measurement of the apparent dissociation constants of carbonic acid in seawater at atmospheric pressure*, Limnol. Oceanogr., 18*, 897-907.

National Research Council. 2010. Ocean acidification: a national strategy to meet the challenges of a changing ocean. *Committee on the Development of an Integrated Science Strategy for Ocean Acidification Monitoring, Research, and Impacts Assessment*. The National Academies Press, 175 pp.

Pierrot, D., E. Lewis, and D. W. R. Wallace (2006), MS Excel program developed for CO_2 system calculations*, ORNL/CDIAC-105.Carbon Dioxide Information Analysis Center, Oak Ridge National Laboratory, US Department of Energy, Oak Ridge, Tennessee*.

Robert-Baldo, G. L., M. J. Morris, and R. H. Byrne (1985), Spectrophotometric determination of seawater pH using phenol red*, Anal. Chem., 57*, 2564-2567.

Sørensen, S.P.L., and S. Palitzsch. (1910). Über die Messung der Wasserstoffionen-konzentration des Meerwassers. Biochem. Z. 24: 387.

Tapp, M., K. A.Hunter, K. Currie, and B. Macaskill. (2000). Apparatus for continuous-flow underway spectrophotometric measurement of surface water pH. *Mar. Chem.* 72: 193–202.

Taylor, B. N. and Kuyatt, C. E.. (1994)*,* Guidelines for Evaluating and Expressing the Uncertainty of NIST Measurement Results. *NIST Technical Note* 1297

Yao, W., X. Liu, and R. H. Byrne (2007), Impurities in indicators used for spectrophotometric seawater pH measurements: Assessment and remedies*, Mar. Chem., 107*, 167-172.

Zhang, H. and R. H. Byrne (1996), Spectrophotometric pH measurements of surface seawater at in-situ conditions: absorbance and protonation behavior of thymol blue*, Mar. Chem., 52*, 17-25.

Chapter 2: A model for biogeochemical cycling in deep mixed layer waters entrained into Subantarctic Mode and Antarctic Intermediate Waters

2.1 Abstract

We develop and employ an inverse model to explore biogeochemical cycling in water from deep wintertime mixed layers entrained into the Subantarctic Mode and Antarctic Intermediate water masses (SAMW and AAIW). Special attention is paid to how this model's parameterization for mixing affects estimates of three biogeochemical processes that are typically estimated using methods that neglect mixing to some degree: shallow calcium carbonate dissolution, Redfield ratios, and initial gas-exchange disequilibrium. The model estimates a shallow (300-700 m) depth calcium carbonate dissolution rate that is roughly half the rate estimated for the Southern Ocean by a similar technique that neglects diapycnal mixing. The model's estimate of the Redfield ratio, $P:N:-O_2:C_{org}/1:(15.2 \pm 0.6):(131 \pm 6):(114 \pm 5)$, has an $-O_2:P$ ratio that differs strongly from many recent global estimates, but agrees well with a separate estimate for this region that allows for diapycnal mixing [*Li and Peng,* 2002] once the effects of anthropogenic carbon uptake are taken into account. We also show that two recent estimates of Antarctic Intermediate Water O_2 and CO_2 disequilibria are not reflected in the Austral winter surface outcropping of the appropriate density surfaces, but are instead interpretable as mixtures between deep mixed layer waters and subsurface components. The model is constructed from a unique dataset collected in the region and season of the deep mixed layers' formation.

2.2 Introduction

In this section we briefly discuss the role that intermediate and mode waters play in global biogeochemical cycling, the processes thought to be responsible for formation of AAIW and SAMW, a dataset that we use to construct a biogeochemical model, and the importance of allowing for multiple dimensions of mixing when modeling biogeochemical processes.

Importance of AAIW and SAMW— The formation of AAIW and SAMW in the frontal region of the Southern Ocean introduces water into the Southern Hemisphere's thermoclines that has recently equilibrated with the atmosphere [*Fine,* 1993*; Fine et al.,* 2001]. These water masses bring comparatively low salinity, low temperature, low alkalinity, and high oxygen content waters northward at intermediate depths and transport freshwater, heat, gases, and nutrients between high and low latitudes [*MacDonald*, 1993]. Intermediate waters also play a significant role in the ocean's uptake of anthropogenic carbon. *Sabine et al.* [2004] estimate that AAIW has an anthropogenic carbon inventory of 20 Pg C, or ~1/6th of their estimated global inventory. Model estimates by *Lovenduski et al.* [2007] and *Lenton and Matear* [2007] suggest that AAIW formation is also responsible for a large fraction of the interannual variability in oceanic anthropogenic CO_2 uptake. Both data and climate models suggest that the formation region for intermediate waters is especially sensitive to climate change [*Bi et al.*, 2002; *Böning et al.*, 2008].

AAIW and SAMW formation mechanisms— Deep mixed layers and regions of high subsurface diapycnal diffusivity are dominant features of the frontal regions associated with AAIW and SAMW formation [*Sloyan et al.,* 2010]. These deep

wintertime mixed layers found between the Subantarctic and Subtropical fronts (SAF and STF) are thought to play an especially significant role in SAMW formation. One paradigm for intermediate and mode water formation, the Mixed Layer Demon Hypothesis [*Stommel*, 1979], suggests that the deepest and densest portions of the deep mixed layers are isolated from the surface by the summertime shoaling of the mixed layers. This water then remains at depth where it may mix into the thermoclines of the Southern hemisphere's gyres. The potential vorticity minimum and the deeper salinity minimum that result from entrainment of this poorly-stratified low-salinity mixed layer water are then the defining characteristics of SAMW and AAIW respectively. While the exact formation mechanisms remain unclear, deep mixed layer waters appear to be a central component of SAMW and, to a lesser-extent, AAIW. The deepest, coldest, and furthest south deep mixed layers are found in the southeastern Pacific sector of the Southern Ocean [*McCartney*, 1977], and this region is thought to be a formation hotspot from which SAMW and AAIW spread into the Pacific and, through the Drake Passage, into other ocean basins [*Sloyan and Rintoul*, 2000].

The AAIW2005 dataset— A hydrographic cruise to the southeastern Pacific during the Austral winter of 2005 has opened possibilities for modeling the biogeochemical processes occurring in AAIW and SAMW. The dataset gathered by this cruise, the AAIW2005 dataset, is novel both for both the location and timing of sampling. Importantly, the dataset contains direct measurements of the deep wintertime mixed layers (DMLs) in the frontal region. The cruise track was chosen to maximize frontal crossings and the sampling of deep mixed layers. Figure 2.1 shows the locations where hydrographic bottle samples were collected superimposed upon extrapolations of the

mixed-layer depths. A profiling 24-Niskin rosette with a CTD was used to collect

samples for salinity (S), phosphate (PO_4^{3-}), nitrate (NO_3^-), silicate ($Si(OH)_4$), oxygen

(O_2), CFCs (11, 12, and 113), carbon tetrachloride (CCl_4), total dissolved inorganic

carbon (C_T), and total alkalinity (A_T). Sample collection was concentrated in the surface

and intermediate depths with approximately 80% of samples collected within the top

1500m.
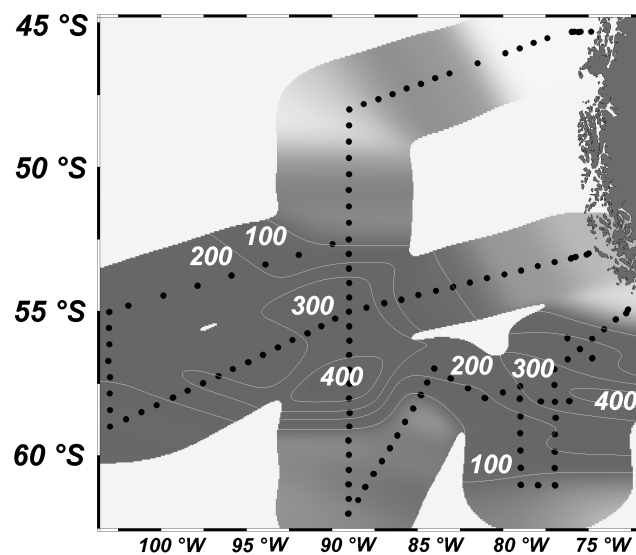
Figure 2.1 A map of the AAIW2005 cruise track. The land mass visible in the northeast corner is Chile. The R/V Knorr departed from Punta Arenas in mid August 2005 and returned to Puerto Montt in early October 2005. Contour lines display extrapolated mixed layer depths determined using a density difference threshold of 0.008 kg m^{-3} γ^n. Black dots indicate stations at which hydrographic bottle samples were collected.

Mixing and biogeochemical estimates— Modeling biogeochemical processes in the ocean requires the ability to distinguish variance in measurements owing to mixing of water masses from variance caused by the processes being modeled. Despite this, the assumption that diapycnal mixing – or indeed all mixing – is a negligible control for property distributions is common to several biogeochemical process estimates. The high diapycnal diffusivities associated with SAMW suggest that these assumptions are especially unlikely to hold for this water mass. In this paper we address bias introduced into estimates of shallow calcium carbonate dissolution, the Redfield ratio [*Redfield*, 1963], CFC ventilation ages, and initial air-sea disequilibrium:

a) Two common approaches for estimating shallow calcium carbonate dissolution rates, the excess calcium [*Kanamori and Ikegami,* 1980] and the TA* approach [*Feely et al.* 2002, 2004], both assume that indicators of dissolution accumulated at the depth at which the measured seawater was collected. Vertical mixing will therefore bias regions of low dissolution signal accumulation – such as the shallow ocean – to higher dissolution rate estimates.

b) The most trusted estimates of the Redfield ratio parameterize for along-isopycnal mixing but neglect diapycnal mixing [*Takahashi et al.,* 1985; *Anderson and Sarmiento,* 1994]. A substantially different $-O_2$:P ratio was obtained by *Li and Peng* [2002] using a multi-parameter linear regression model that implicitly allowed for diapycnal mixing.

c) *Sonnerup* [2001] and *Mecking et al.* [2004] have demonstrated that subsurface mixing biases CFC age estimates due to CFCs' non-linear atmospheric growth histories.

d) Mixing complicates the interpretation of preformed air-sea gas disequilibria. It is unclear whether the estimated disequilibria are due to poorly-equilibrated surface water masses subducting or the mixture of a mostly-equilibrated water mass with an underlying water mass.

2.3 Methods

Here we present an inverse model designed to examine the effects of mixing, gas exchange, and biological activity on deep mixed layer water entrained into the AAIW and SAMW masses. We describe the model's construction from the AAIW2005 dataset and then discuss model output uncertainties resulting from uncertainties in model assumptions and in the data used.

2.3.1 Model construction

Model overview— The inverse model relies upon three central assumptions regarding the behavior of mixtures between the entrained deep mixed layers and other water masses. These assumptions treat the non-DML water masses as "mixing correction" terms and not as true "endmember" components with a supposed initial surface expression. Collectively, these assumptions eliminate the need to back estimate what the properties of the pure surface of endmember components would have been (necessary since endmember property distributions that are determined using water that has already been subjected to a process will underestimate the influence of that process) as well as the necessity of assuming that mixing occurred either entirely at the time of water mass formation or entirely in the moment before it was measured (otherwise

necessary to determine to what degree accumulated signal has been diluted by subsequent mixing):

a) Processes that control the property distribution of a component that mixes with entrained DML waters also control the properties of the fraction of that component in the mixture with DML water.

b) The DML component's property distribution – characterized using measurements of this water at the ocean's surface – reflects the initial properties of this water as it is entrained into SAMW and AAIW.

c) The property distribution of the other components that mix with the DML component are the result of unknowable mixing, gas exchange, freshening, secular warming, and biological processes.

The model allows for property perturbations from mixing with water masses found above and below the SAMW and AAIW masses: Subtropical Surface Water (SSW), found atop the mode water tongue north of the STF, and Upper Circumpolar Deep Water (UCDW), found below the AAIW mass and upwelling south of the Polar front (PF). These assumptions collectively imply that any biogeochemical signals that are observed after accounting for mixing with these components can be attributed to the DML component and to processes acting solely upon it (see the Appendix to this chapter for further discussion related to these assumptions).

The model takes four steps to estimate processes responsible for each sample's property distribution:

(1) Component fractions are fit to the measured salinity and calculated potential temperature.

(2) The DML's CFC concentrations are inferred from the difference between the measured CFC concentration and the amount attributed to mixing with other components, and these are used to estimate the DML component's ventilation date. A parameterization for long term warming and freshening (see below) returns iteratively to step (1) at this stage.

(3) The C_T of the DML component is estimated with equilibrium equations, historical records of atmospheric partial pressures, and the CFC ventilation date estimate.

(4) Remaining discrepancies between modeled and measured concentrations are attributed to the action of the hard and soft tissue pump on the DML component. Concentration gains are regressed against age and one another to determine remineralization rates and Redfield ratios.

Component property distributions— Water mass property distributions are defined by averaging the measured properties of samples collected from mixtures between the desired water masses and DML waters. Property distributions obtained in this manner for the two mixing components simply define mixing trends for the measured properties. Without pure endmember property distributions for these mixing components, water that is less than 0% made up of any given component – and hence more than 100% composed by the other two components – is physically plausible. However such water is outside of the scope of this model and is neglected in our analyses.

The DML component is only characterized with data from samples collected within a mixed layer (defined with a neutral density threshold 0.008 kg m^{-3} γ^n) of >300 m depth. Latitude and longitude restrictions are used for the definition of all components to

ensure that data are not overly affected by landmass runoff and are appropriate to the

region and processes being modeled. The UCDW and SSW components are intentionally

chosen from water masses that are likely to be partially composed of the DML

component. This limits the scope of the model to the data between the regions in which

these data is used to define the mixing components, but it also reduces the chance that the

endmembers also reflect the effects of mixing with other water masses that are unrelated

to SAMW and AAIW (refer to the Appendix of this Chapter for further discussion on this

issue). The SSW component is identified using data from a shallow subsurface salinity

maximum found just above the shallowest neutral density surfaces that connect to the

deep mixed layers. The UCDW component is defined above a potential vorticity

maximum found near 1000 m.
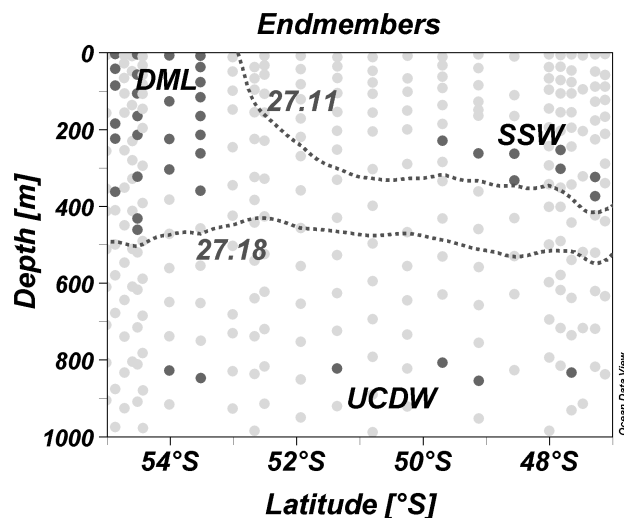
Figure 2.2 A plot of data between 85-90 ºW and 0-1000 m depth showing locations of hydrographic data collection (all dots). Constant neutral density contour lines of the densest and least-dense DML waters are shown as dotted lines. Dark grey dots indicate data included in the averaging process for the three (labeled) components. Light grey dots indicate locations where data is present.

We use the following criteria to select data representative of the water masses:

DML: Inside DMLs; Longitude > 86° W; Latitude < 55° S;

SSW: Longitude > 86° W; $S < 34.1$; $\Theta > 5$ °C

UCDW: Longitude > 86° W; 4.1 °C < Θ < 4.2 °C; Depth > 500 m

Bottles missing one or more measurements of relevant properties are excluded from the averaging process for all of the properties to avoid biasing component property definitions relative to one another. Figure 2.2 shows the latitude and depth of all points included for each of the three components. Table 2.1 lists the averaged property distributions for all three components.

Table 2.1 Component property distributions.

Property	Units	DML	SSW	UCDW
Θ	°C	5.243	5.878	4.127
S	-	34.178	34.252	34.271
Oxygen	μmol kg^{-1}	299.9	274.6	218.8
Nitrate	μmol kg^{-1}	20.16	21.60	29.99
Phosphate	μmol kg^{-1}	1.43	1.52	2.07
CFC-11	pmol kg^{-1}	4.64	4.34	2.27
CFC-12	pmol kg^{-1}	2.56	2.37	1.15
C_T	μmol kg^{-1}	2121.1	2131.8	2186.6
A_T	μmol kg^{-1}	2273.0	2274.7	2290.0

Estimating component fractions— Mixing fractions are estimated for a water parcel using mass, salinity, and potential temperature conservation. These relationships can be written as:

$$1 = f_1 + f_2 + f_3 \tag{1}$$

$$S = f_1 S_1 + f_2 S_2 + f_3 S_3 \tag{2}$$

$$\Theta = f_1 \Theta_1 + f_2 \Theta_2 + f_3 \Theta_3 \tag{3}$$

Here f denotes the component mixing fraction, S refers to salinity, Θ refers to potential temperature, subscripts denote which component the mixing fraction or property applies to (1 to DML, 2 to SSW, and 3 to UCDW), and a property without a subscript refers to a measured value for the seawater being modeled. These equations are rearranged to solve for the mixing fractions:

$$f_3 = \frac{\left(\dfrac{S - S_1}{S_1 - S_2} + \dfrac{\Theta_1 - \Theta}{\Theta_1 - \Theta_2} \right)}{\left(\dfrac{S_3 - S_1}{S_1 - S_2} + \dfrac{\Theta_1 - \Theta_3}{\Theta_1 - \Theta_2} \right)} \tag{4}$$

$$\tag{5}$$

$$f_1 = 1 - f_2 - f_3 \tag{6}$$

It is useful to define a separate term that refers to the estimated value of a property that a parcel of water would have if mixing were the only influence on that property:

$$X' = X_1 f_1 + X_2 f_2 + X_3 f_3 \tag{7}$$

Here X' refers to the mixing-only estimate for a hypothetical property X. Since the mixing model is exactly determined (3 relationships with 3 unknowns), the "mixing" potential temperature and salinity are necessarily equal to the measured potential temperature and salinity.

Parameterization for gas exchange— The concentrations measured in the DML component in 2005 may not reflect the concentrations of previous years' DMLs for properties with a growing atmospheric concentration (C_T, CFC-11, CFC-12). This is addressed by replacing the averaged concentration of that species in the DML component with a time-sensitive gas-exchange equilibrium value of that property:

$$X'' = eX_1(S_1, \Theta_1, p(X)(t))f_1 + X_2 f_2 + X_3 f_3 \qquad (8)$$

Here e is the degree of saturation of the gas in the averaged DML component expressed as a fraction and $X_1(S_1, \Theta_1, p(X)(t))$ is the equilibrium concentration of gas X at the DML's measured salinity S_1, the DML's measured potential temperature Θ_1, and the changing atmospheric partial pressure of the gas $p(X)(t)$. The double prime on X'' indicates that this mixing estimate is also parameterized for gas exchange with an atmosphere with a variable atmospheric concentration. We assume the CFC and CO_2 partial pressures match the atmospheric record measured at the Tasmanian Cape Grim Baseline Air Pollution Station. We use the oxygen, CFC, and carbonate system equilibrium constants provided by *Garcia and Gordon* [1993], *Warner and Weiss* [1985], and *Dickson and Millero* [1987] respectively. We also employ the CO2SYS routine written for Matlab by *Van Heuven et al.* [2009].

It is not clear that our assumption of constant C_T disequilibrium over time is appropriate for this region. Given that the deep mixed layers are generally supersaturated with respect to C_T as a result of entrainment of deeper high $p(CO_2)$ waters, increasing atmospheric $p(CO_2)$ should act to decrease the deep mixed layer air-sea C_T disequilibrium over time. To address our lack of confidence in this parameter, we assess the sensitivity of the $R_{C:P}$ to a changing air-sea disequilibrium with additional model runs with an extra term to reflect this possibility. The term is applied as an offset to C_T that scales linearly with the year of the DML component's subduction (the year of ventilation is estimated using the procedure described below).

CFC ventilation date estimates— The CFC measurements are used to estimate ventilation dates for the DML components of water mixtures by finding the optimal dates

to satisfy equation (8) for the two CFCs. This "mixing" ventilation date estimate is distinct from the "traditional" approach to CFC dating both in method and in interpretation. The mixing approach estimates the date that the DML component lost atmospheric contact whereas the traditional approach, obtained by optimizing equation (9):

$$[CFC-12]_1(S_1, \Theta_1, p(CFC-12)(t)) = [CFC-12] \qquad (9)$$

estimates the mean date that a mixture of water masses lost contact. We do not include a disequilibrium parameter for these ventilation date estimates since the water mixtures have no unambiguous single source region. CFC subduction dates are also calculated using the traditional formulation for comparison, and both sets of results are presented. The distinct shapes of the two CFC atmospheric growth histories make each better suited for ventilation date estimates from specific time intervals. To ensure that each CFC measurement returns only a single ventilation date estimate, we fit measurements using the CFC-12 growth curve from 1940 to 2003 and the CFC-11 decay curve from 1995 to 2006. Values from the decaying portion of the atmospheric CFC-11 curve are reported when CFC-12 estimates yield dates of ventilation more recent than 1998. We estimate ventilation dates, but discuss ventilation ages. These are determined straightforwardly by subtracting the ventilation date from the cruise date (2005.75 c.e.).

Biological effects— Any remaining differences between the measured properties and the properties and the properties estimated from equations (7) and (8) are attributed to the effects of biology. Changes resulting from the soft tissue pump (organic matter) are assumed to obey a single Redfield ratio for this entire region. We account for the effect of the soft tissue pump on A_T (through the release of protons during organic matter

remineralization) using an adjustment based upon the approach used by *Brewer et al.*
[1975]. The adjustment is incorporated into the Redfield ratio by assuming:

$$R_{A:P} = -(1 + R_{N:P}) \tag{10}$$

Here $R_{N:P}$ refers to the ratio of the change in nitrate to the change in phosphate resulting

from the soft tissue pump. An additional term is included to allow for the effects of the

hard tissue pump ($CaCO_3$ transport) on A_T and C_T. The effects of the hard tissue pump

on alkalinity are twice the effects on C_T since the dissolution of a single unit of calcium

carbonate increases C_T by one unit and alkalinity by two units.

Given these formulations for mixing, gas exchange, and biology, property budgets

for the individual chemical species are then:

$$[PO_4^{3-}] = [PO_4^{3-}]' + sf_1 \tag{11}$$

$$[NO_3^-] = [NO_3^-]' + sf_1 R_{N:P} \tag{12}$$

$$[Si(OH)_4] = [Si(OH)_4]' + sf_1 R_{Si:P} \tag{13}$$

$$[O_2] = [O_2]'' + sf_1 R_{O:P} \tag{14}$$

$$A = A' + 2hf_1 - sf_1(1 + R_{N:P}) \tag{15}$$

$$C = C'' + hf_1 + sf_1 R_{C:P} \tag{16}$$

$$[CFC\text{-}11] = [CFC\text{-}11]'' \tag{17}$$

$$[CFC\text{-}12] = [CFC\text{-}12]'' \tag{18}$$

Here s is the concentration change of phosphate resulting from the soft tissue pump and

h is the change in the concentration of dissolved inorganic carbon resulting from the hard

tissue pump.

Hard and soft tissue pump rate estimates— Equations 10-13 are rearranged to solve for the amount of organic matter remineralization and calcium carbonate dissolution that has occurred in the DML component:

$$s = \frac{[PO_4^{3-}] - [PO_4^{3-}]'}{f_1} \tag{19}$$

$$h = \frac{A + [NO_3^-] + [PO_4^{3-}] - A' - [NO_3^-]' - [PO_4^{3-}]'}{2f_1} \tag{20}$$

Rate estimates are also made for these processes using the age of the DML component of that water parcel. Rates of organic matter remineralization and calcium carbonate dissolution are obtained by fitting linear trends of the form:

$$s = r_S a \tag{21}$$

$$h = r_H a \tag{22}$$

relating water parcel age estimates to total remineralization and dissolution estimates. Here a represents the estimated CFC age for the DML component in that parcel and r_S and r_H refer to the rate of the hard and soft tissue pump. The structure of this model limits its scope to water parcels that show a distinct DML component, that are unlikely to be mixed with the deep mixed layers of successive years. Therefore estimates from water collected south of 55° S or at less than 300 m depth are excluded from these averages. Additionally, data with an estimated DML component that is less than 0.3 (< 30% composed of DML) are excluded to limit the amplification of errors associated with small denominators in equations (19) and (20).

Redfield Ratios— Redfield ratios for the soft (and hard) tissue pump are estimated by regressing biologically accumulated C_T, oxygen, silicate, and nitrate against biologically accumulated phosphate. This regression fits linear equations of the form:

$$[NO_3^-] - [NO_3^-]' = R_{N:P}(sf_1) \tag{22}$$

$$[O_2] - [O_2]'' = R_{O2:P}(sf_1) \tag{23}$$

$$C - C'' - hf_1 = R_{C:P}(sf_1) \tag{24}$$

The data used for the regressions in equations (22) through (25) are restricted to measurements indicating positive mixing fractions for all three components made north of 55 ºS, and deeper than 300 m. For $R_{C:P}$ values estimated using mixing ages, the additional requirement of a DML component greater than 0.3 is imposed to ensure viable mixing CFC dates. A similar treatment is applied to silicate's covariance with the hard tissue pump by fitting a linear equation of the form:

$$[Si(OH)_4] - [Si(OH)_4]' = R_{Si:h}(hf_1) \tag{25}$$

Parameterization for variability of the DML component— Climate change and observations of the freshening and warming of the surface of the Southern Ocean [*Böning et al.,* 2008] challenge the assertion that the DML property distributions measured in 2005 are representative of DML property distributions from other years. If the DML component were cooler and more saline in the past, a model constructed using modern data would underestimate the contribution of DMLs to the water parcels considered. A separate set of modified model runs were conducted to address the effects of a warming and freshening DML component on the model outputs. This model begins with the

estimation of traditional CFC dates for each water parcel. The warming and freshening

trends estimated by *Böning et al.* [2008] are then used to back-estimate what the physical
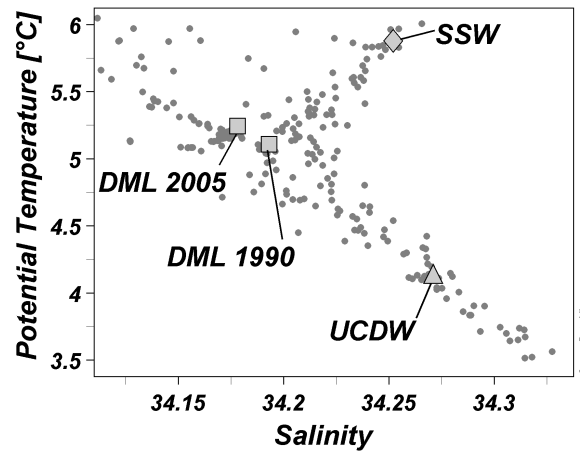
Figure 2.3 Plot of Θ versus salinity for data between 85-90 °W and 300-750 m depth. Component properties are shown as squares (DML), a diamond (SSW), and a triangle (UCDW). The second square, labeled DML1990, shows the estimated DML property distribution of 1990 assuming the warming and freshening patterns found by *Böning et al.* [2008] are extrapolated backwards in time. Individual data points are plotted as dark grey dots.

properties of the DMLs would have been in those years. These trends were estimated by

Böning et al. [2008] using data collected in this region from 300-1000 m depth and from

1980 to 2008 (warming of 0.009 ± 0.001 °C yr^{-1} and a salinity freshening of $-0.0010 \pm$

0.0004 yr^{-1}). Figure 2.3 is a plot of Θ versus salinity with the modern components plotted

and with an estimate for what the DML component would have been in 1990 if it

followed these trends. The DML component's A_T is also adjusted by the same fraction as

the salinity to account for the expected effects of freshwater dilution on this parameter.

This adjusted property distribution for the DMLs is then used to generate mixing ratios,

mixing dates, and outputs. This process is repeated iteratively using mixing dates to

adjust component parameters and component parameters to estimate mixing dates until successive component fraction estimates agree to within 0.01% for all data points. This modification of the model is referred to as the "warming model," and the unmodified version is referred to as the "static model." Results from both models are given, but discussion is limited to the warming model results.

Coastal influences— Sedimentary organic matter degradation and land runoff are additional complicating factors for shallow and near-shore stations. We explore the effect that these processes have on our estimates by repeating the warming mixing model analysis for this dataset after subdividing it along 85 ºS. Except when specified, model results discussed are those obtained using the entire dataset.

2.3.2 Output uncertainties

Here we describe a pair of methods we employ to assess the *minimum* model output uncertainties that apply beyond model output uncertainties uncovered by the sensitivity analyses noted above (and uncertainties from any unaddressed assumption errors).

Single process set method— The first method tests the assumption that there is only a single set of processes acting upon the DML components in each mixture at fixed rates. We assume that variability in process rate estimates (and in the ratios between them) represents uncertainty inherent to the model and this assumption. For Redfield ratios and the soft and hard tissue pump rates these uncertainties are expressed as ±95% confidence intervals for the value of the slope of the line being fit to the data. These uncertainties are given with the results.

Table 2.2 Assumed and estimated uncertainties (standard deviations).

Input Term	Units	Error	Output Term	Units	Monte Carlo *Warming*
Θ	°C	0.002	DML	-	0.043
S	-	0.002	SSW	-	0.015
$[O_2]$	µmol kg^{-1}	1.5	UCDW	-	0.031
$[Si(OH)_4]$	µmol kg^{-1}	0.04	a (mix)	yr	0.99
$[NO_3^-]$	µmol kg^{-1}	0.04	a (trad)	yr	0.47
$[PO_4^{3-}]$	µmol kg^{-1}	0.01	r_S (mix)	µmol kg^{-1} yr^{-1}	0.0004
CFC-11	pmol kg^{-1}	0.05	r_S (trad)	µmol kg^{-1} yr^{-1}	0.0003
CFC-12	pmol kg^{-1}	0.025	r_H (mix)	µmol kg^{-1} yr^{-1}	0.01
C_T	µmol kg^{-1}	1.7	r_H (trad)	µmol kg^{-1} yr^{-1}	0.01
A_T	µmol kg^{-1}	1.3	$R_{N:P}$	-	0.2
			$R_{Si:h}$	-	0.02
			$R_{O2:P}$	-	2
			$R_{Corg:P}$ (mix)	-	2
			$R_{Corg:P}$ (trad)		2

Monte Carlo estimate— The second method uses a Monte Carlo analysis to determine how imprecision in the data propagates through to imprecision in the model outputs. First, each measurement in the dataset is perturbed by a random offset selected from a population with a normal distribution about zero and a standard deviation equal to the estimated measurement deviation for that parameter in the AAIW2005 dataset. The model is then rerun using the perturbed data and a new set of estimates is recorded. This procedure is repeated 500 times to obtain this many model result sets. The standard deviation of the model results in this set is then assumed to reflect the uncertainty in the model outputs that results purely from uncertainty in the data. For mixing fractions and CFC ages (estimated for each data point within a dataset) the deviation of the population of the differences between the perturbed model estimates and the original model estimates are considered. Assumed uncertainties for AAIW05 data and the resulting

uncertainties of model outputs (estimated with this method) are given as standard deviations in Table 2.2.

Summary— The uncertainties estimated using the Monte Carlo approach are smaller than the uncertainties estimated using the single-population approach after accounting for differences in how the terms are expressed (deviation vs. confidence interval). The Monte Carlo analysis uncertainty estimates can be interpreted as a lower bound on the uncertainties of the model resulting from uncertainties in the data. The "single process set" estimates can be interpreted as a lower bound on the uncertainty resulting from uncertainties in the data and in the model assumptions.

2.4 Results and Discussion

2.4.1 Component fractions

The distribution of components only has physical meaning to the degree that the components indeed reflect pure endmembers. That said, component distributions are important to consider since the uncertainty introduced to process rate estimates by assumptions is much greater for water masses with smaller DML components. This is doubly true for estimates obtained using "mixing ages." Predicted component distributions also provide a tool to check whether predicted mixing patterns make sense in the context of observed property distributions.

Figure 2.4 shows the distribution of mixing estimates for each of the three components for both the warming model and the static model. These distributions have several notable features: First, DML component fraction estimates indeed reach a maximum at intermediate depth. Secondly, DML estimates also are higher near 55 ºS

DML Component Fraction
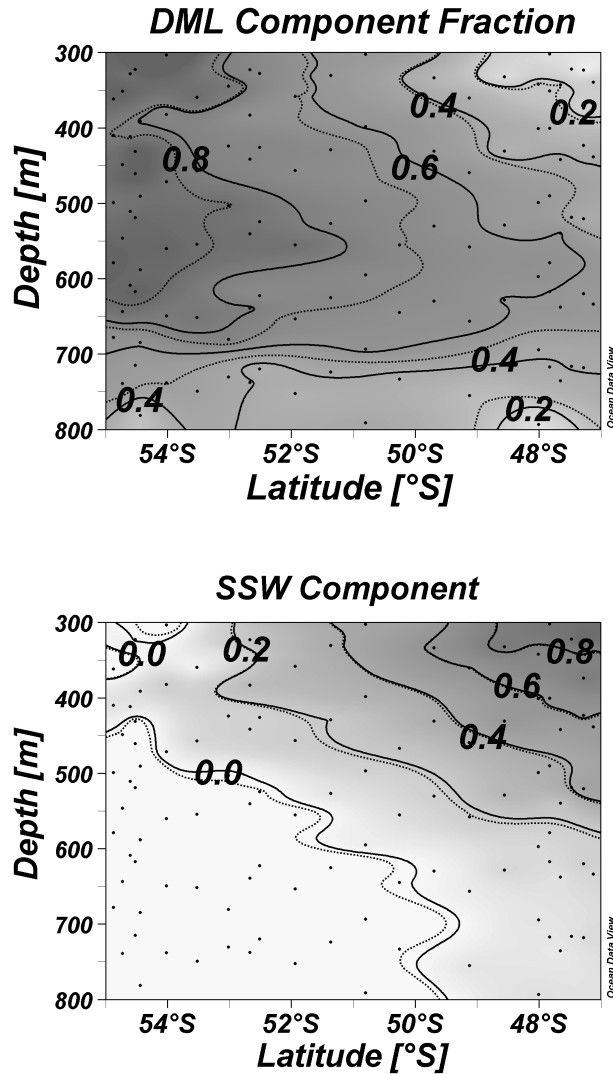
SSW Component

Figure 2.4 Shading and contours indicate component fraction distributions estimated with the static and mixing models between 85-90 °W and 300-750 m depth. Unlabeled dotted contour lines indicate contours for static model mixing fractions. These share the larger adjacent solid contour's value for the warming SSW fraction and the smaller adjacent value for the warming DML fraction. Black dots indicate where sufficient data is present to obtain mixing fraction estimates.

than near 48 °S. Both of these observations are consistent with the supposed pattern of

mixing for this water mass and indicative of subsequent mixing of significant fractions of

UCDW and SSW. Third, the warming model estimates larger DML fractions than the

static model. This is most pronounced in areas that are deeper and areas that are further from 55 °S. As is discussed in the next section, these areas are also the areas with the oldest mixing CFC ages. The comparatively larger DML fractions therefore make sense given that the effects of a warming correction applied to modern DML data would be most pronounced for the oldest age estimates. This results in a markedly deeper estimated DML maximum for the warming model than for the static model.
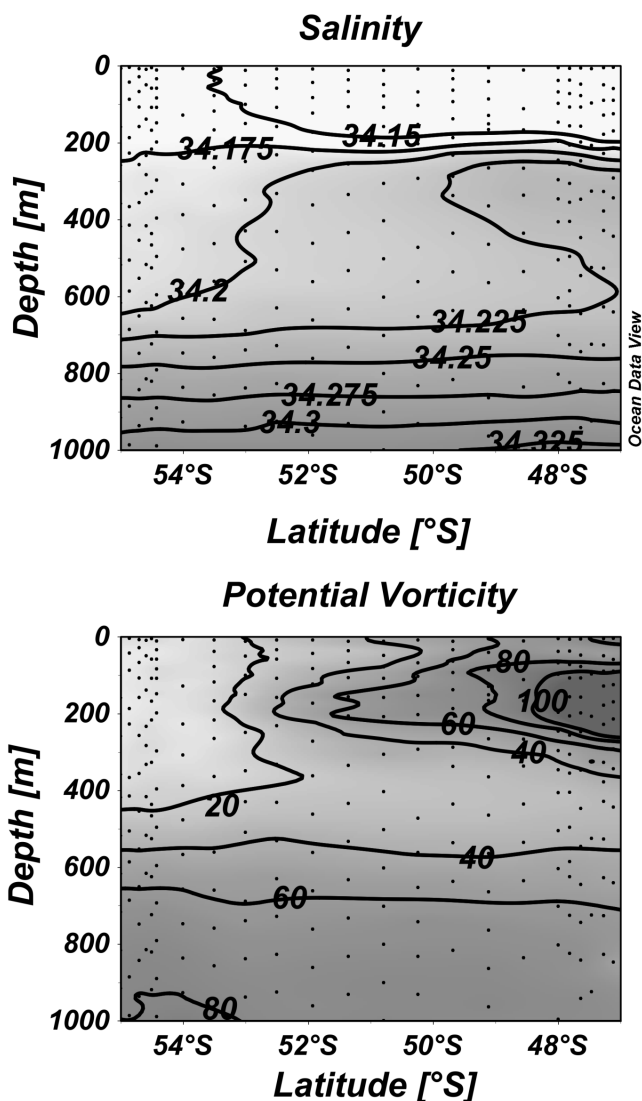
Figure 2.5 Potential vorticity (expressed as 10^{-12} m^{-1} s^{-1}) and salinity distribution observed between 85-90 °W and 300-750 m depth.

The potential vorticity minimum found between 400 and 500 m depth and the salinity minimum found between 500 and 600 m are shown for this region in Figure 2.5. Contrary to expectation, predicted DML component distributions match up better with the salinity minimum associated with AAIW than with the potential vorticity minimum associated with SAMW. This can be explained as an artifact of how components are defined: the requirement that the SSW component be defined using data that is out of contact with the surface necessitates using measurements from water with an average neutral density very similar to the least dense DML data. By contrast, the UCDW component is defined using significantly denser water than the densest DMLs. This should result in an artificially deep DML component maximum. Biogeochemical process estimates will therefore be most appropriate for the 400–700 m depth interval where a significant DML component is found.

2.4.2 CFC age estimates

The traditional CFC ages and the two sets of mixing CFC ages – estimated by the warming and static models – are shown along 90 °W in Figure 2.6. Figure 2.7 directly compares mixing ages with traditional ages for both the warming model and the static model. These figures show that mixing estimates are generally younger than traditional estimates for these sections of the AAIW and SAMW masses. The difference is most pronounced ($\Delta > 10$ years) in shallow younger waters due to the absence of a disequilibrium term for the traditional ages. This observation can be understood either by allowing that the DML component in these mixtures is younger than the average age of

the waters with which it is mixed or that the surface ocean is significantly out of

equilibrium with the atmosphere.
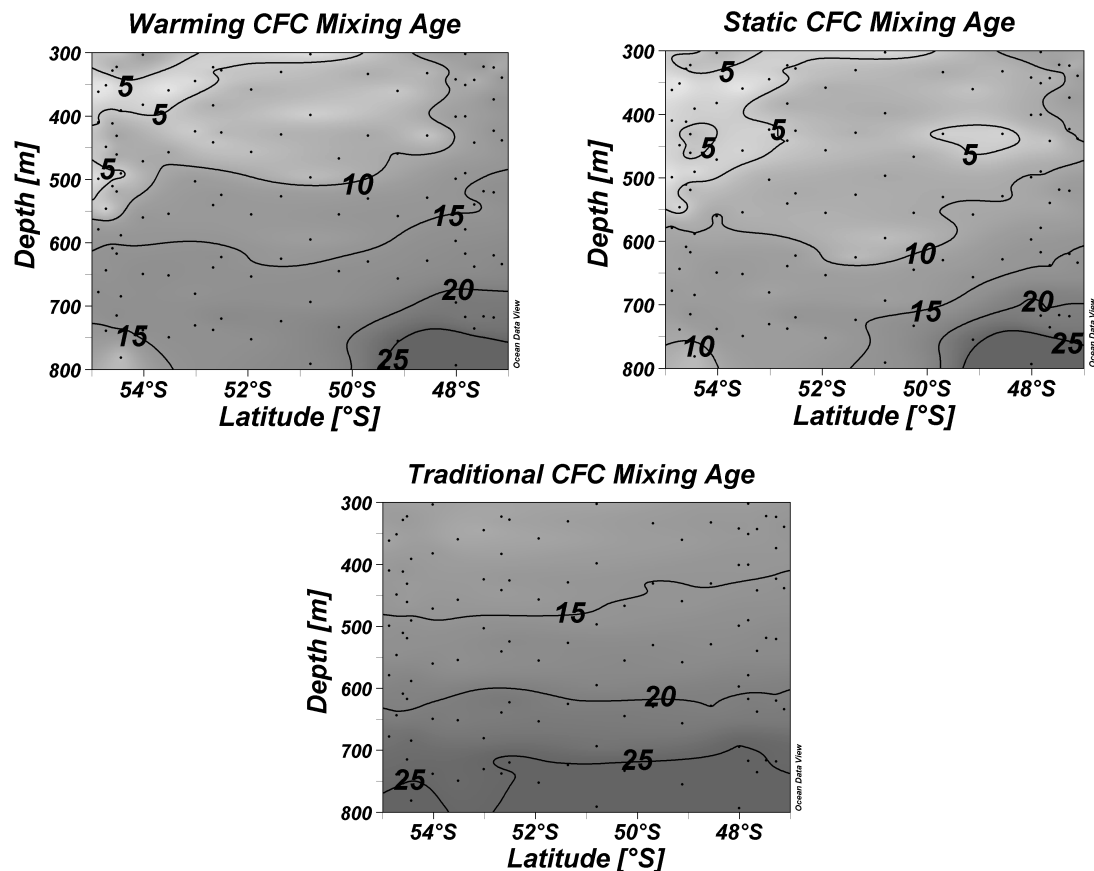
Figure 2.6 Distribution of mixing and traditional CFC ages for the static and mixing models between 85-90 ºW and 300-750 m depth. Data for which all measurements were available are shown as black dots. The traditional CFC ages are unaffected by the mixing model, so only one estimate distribution is shown.

It is difficult to judge whether mixing ages correctly adjust for the bias introduced

by linear mixing of points along a non-linear atmospheric growth curve as described by

Sonnerup [2001]. In order to directly compare mixing and traditional ages, we consider a

mixing-fraction-weighted mean mixing ventilation date by assuming that SSW and

UCDW were last ventilated in their apparent traditional CFC ventilation dates of 1989

and 1977 respectively. These weighted mean mixing ages are generally older than

traditional CFC ages (by 1.0 ± 0.3 y (s); d.f. = 26) for mixtures with a traditional CFC age older than 1988 and younger (by 2.4 ± 2.8 y (s); d.f. = 23) for mixtures with a traditional CFC age younger than 1990. These offsets are generally in opposition to the mixing biases estimated by *Mecking et al.* [2004] for the North Pacific.
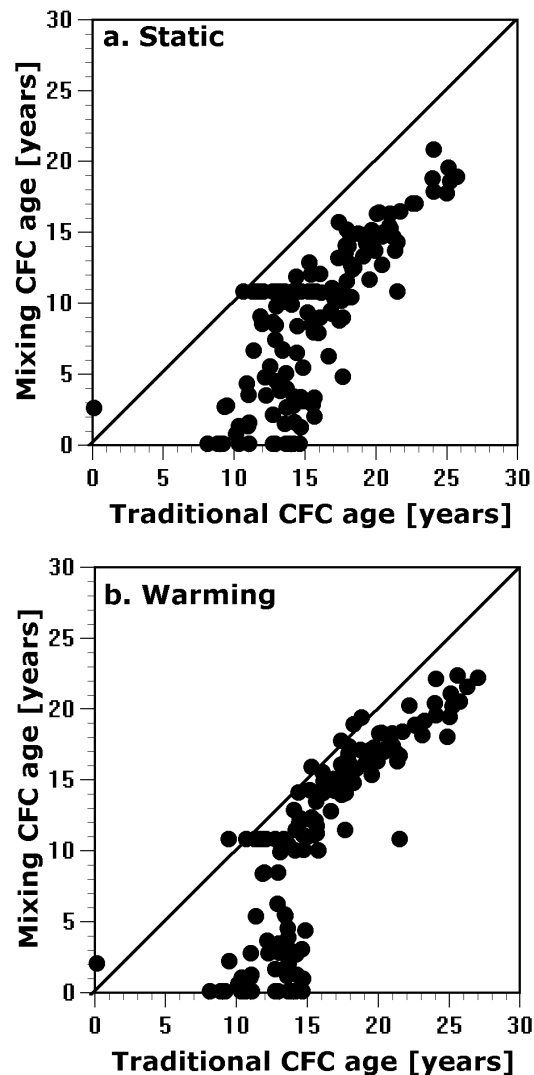
Figure 2.7 A plot of estimated mixing CFC ages against traditional CFC ages. Only data for which there is also a distinct DML fraction (>0.3) and a positive SSW and UCDW fraction are shown.

Two strong limitations will prevent mixing ages from being widely applicable in the oceans: they are only conceptually viable in regions that contain a significant fraction

of a distinct subducting surface component and it is necessary to have that component well-characterized in the season in which it subducts. The mixing age approach is thought to be the better estimate of how long the DML component has been entrained for the purposes of this model however. Results obtained using both types of age estimates are presented, but discussion is limited to results obtained from mixing ages.

2.4.3 Hard and soft tissue pump rates

Estimates of the rate of phosphate release by the soft tissue pump, the rate of carbon release by the hard tissue pump, and the Redfield ratios are given in Table 2.3. The estimated phosphate remineralization rate is 0.018 ± 0.002 μmol kg^{-1} yr^{-1}. This is smaller than estimates obtained using the M.2 and M.02 models for these depths for the global ocean by *Anderson and Sarmiento* [1995] and for the North Atlantic by *Sarmiento et al.* [1990]. It is comparable to the fitted carbon and nitrogen regeneration rates obtained from sediment traps for the composite of open ocean sites given by *Martin et al.* [1989] when these rates are calculated to a depth of 300 meters. It is larger than the 0.03 μmol N$_{org}$ kg^{-1} yr^{-1} (~0.002 μmol P$_{org}$ kg^{-1} yr^{-1}) sediment trap based organic nitrogen regeneration rate given by *Wong et al.* [1999] for the depth range from 200 to 1000 m at Ocean Station Papa. Naturally, these direct comparisons cannot be overly interpreted since these other regions reflect different depths in the water column and different biological communities. Two studies have deployed sediment traps within the Subantarctic Zone of the Southern Ocean, but they do not have records from tethered drifting traps that allow estimation of remineralization rates in the top 1000 meters [*Honjo et al.,* 2000*; Trull et al.,* 2001]. However, they do indicate a comparable N$_{org}$

transport across the 1000 m depth threshold to the transport found at this depth at Ocean

Station Papa by *Wong et al.* [1999].

Table 2.3 Process rates, Redfield ratios, and confidence intervals.

Term	Warming DML			Static DML		
	Value	*± (95%)*	*N*	*Value*	*± (95%)*	*N*
s rate (mix)*	0.018	0.003	84	0.019	0.004	57
s rate (trad)*	0.016	0.003	92	0.011	0.003	92
h rate (mix)*	0.14	0.02	84	0.07	0.03	57
h rate (trad)*	0.14	0.02	92	0.04	0.02	92
$R_{N:P}$	15.2	0.6	99	14.6	0.8	78
$R_{Si:h}$	1.20	0.12	99	0.68	0.20	78
$R_{-O2:P}$	131	6	99	132	9	78
$R_{Corg:P}$ (mix)	114	5	84	101	8	57
$R_{Corg:P}$ (trad)	118	6	92	114	9	92

* units are μmol kg^{-1} yr

This model's estimate of the calcium carbonate dissolution rate is 0.14 ± 0.02

μmol CaCO$_3$ kg^{-1} yr^{-1}. This value is near the lowest end of the 0.3 ($\pm$ 50%) μmol CaCO$_3$

kg^{-1} yr^{-1} dissolution rate estimated by *Berelson et al.* [2007] using the TA* method for

200-1500 m depth range of the entire Southern Ocean. The TA* method suggests a

higher local dissolution maximum over the subset of this depth range considered by this

model (~300 to 750 m depth) than for the 200-1500 m depth range for most ocean basins

[*Feely et al.,* 2004]. However, TA* values are actually negative over this depth region of

the Southern Ocean in both the AAIW2005 dataset and the GLODAP dataset used by

Feely et al. [2002]. The TA* method attributes negative values to uncertainties in the

preformed potential alkalinity estimates and sets them to zero. The TA* method is

therefore likely to be most effective when estimating global averages, and should be

interpreted with caution on a regional level. We attribute our estimate's value being both

positive and lower than *Berelson et al.* [2007]'s mean estimate for the Southern Ocean to

our model's parameterization for mixing processes.

Friis et al. [2006] use a global circulation model to show that the observed global TA* distribution can be reproduced with calcium carbonate dissolution occurring exclusively in deeper undersaturated waters if vertical mixing is allowed. A similar conclusion is reached for the North Atlantic in *Friis et al.* [2007]. While our estimates are lower than the TA* method's, we do find that statistically significant calcium carbonate dissolution is occurring above the aragonite saturation horizon.

Shallow water sediment traps provide another means of estimating shallow carbonate dissolution rates, though this method is considered to be unreliable [*Buesseler, 1991; Yu et al.,* 2001]. One deployment in the Northern Pacific found less particulate inorganic carbon attenuation with depth than predicted by the TA* method [*Wong et al.,* 1999]. *Berelson et al.* [2007] indicate that the TA* method suggested a 1.7 mmol m^{-2} d^{-1} (~0.5 µmol kg^{-1} yr^{-1}) dissolution rate in this region where only 0.23 mmol m^{-2} d^{-1} (~0.07 µmol kg^{-1} yr^{-1}) was found. This region is not strictly comparable with the Southern Ocean however, as *Wong et al.,* [1999] also found considerably less CaCO$_3$ at 1000 m depth in the North Pacific than has been found at this depth in the subantarctic zone (2.6 g m^{-2} yr^{-1} in the North Pacific vs. 5.1 g m^{-2} yr^{-1} in the Southern Ocean) [*Trull et al.,* 2001]. If the shallow-depth dissolution rate scales linearly with the fluxes across the 1000 m threshold, this sediment trap data would suggest a shallow water dissolution rate of 0.14 µmol kg^{-1} yr^{-1} when scaled to the 1000 m CaCO$_3$ flux of the Southern Ocean. This value is indistinguishable from our dissolution rate estimate for this region.

Extrapolating our estimated dissolution rate of 0.14 µmol CaCO$_3$ kg^{-1} yr^{-1} to the entire Southern Ocean using an ocean area of 3.6×10^{13} m^2 and a shallow depth range of 200-1500 m gives an estimate of 0.079 Gt particulate inorganic carbon (PIC)

remineralized above the saturation horizon annually. This value is roughly 50% of the

value estimated by *Berelson et al.* [2007] using TA*. Our estimate might also be an

overestimate for the entire Southern Ocean as *Honjo et al.* [2000] report that the latitudes

modeled exhibit higher PIC fluxes at depth than regions further south. However, the TA*

overestimation we suggest for this region might also be considered a high estimate of the

additional uncertainty introduced to these methods from mixing since the SAMW mass

has abnormally high diapycnal diffusivity [*Sloyan et al.,* 2010]. Overall, these findings

support the statement by *Friis et al.* [2006] that calcium carbonate dissolution tracers that

do not take into account mixing will overestimate shallow depth calcium carbonate

dissolution.

A decreased estimate of shallow calcium carbonate dissolution rates could have

profound implications for our interpretations of global alkalinity budgets. For instance,

Berelson et al. [2007] suggest that their global average export flux estimate of 1.6 GtPIC

yr^{-1} would be revised to 1.1 GtPIC yr^{-1} if shallow calcium carbonate dissolution were

overestimated by 50%.

2.4.4 Redfield ratios

The estimated Redfield ratios are P:N:$-O_2$:C_{org} /1:(15.2 ± 0.6):(131 ± 6):(114 ±

5),. Our estimates for N:P and $-O_2$:P are similar to those obtained by *Li and Peng* [2002]

for the same region (1:(15 ± 1):(−133 ± 5):(80 ± 3)), though our ratios of C_{org}:P are quite

different. These estimates both use 3 component mixing strategies for this region, though

Li and Peng [2002] are able to avoid explicitly defining their components due to the

scope of their analysis. It is reassuring that the estimated ratios are similar for these techniques given this difference.

We explain the differences in the organic carbon to phosphate remineralization ratios using the mechanism proposed by *Körtzinger et al.* [2001] who showed that anthropogenic carbon uptake gradients bias organic carbon Redfield ratios low in the Northeast Atlantic by 25-30%. *Li and Peng* [2002] did not parameterize for anthropogenic carbon uptake while including data as shallow as 100 m in their MLR analysis, and it is therefore likely that their data is influenced by anthropogenic carbon. Indeed, their analysis of the global ocean predicts low C_{org}:P ratios only in the areas that are most influenced by anthropogenic carbon uptake (North Atlantic and the Southern Ocean) and higher ratios in regions that are the least influenced (C_{org}: P ratio of 124 in the North Pacific). Without the anthropogenic carbon parameterization, our model estimates a C_{org}:P ratio of 76 ± 5 which is similar to the Southern Ocean value from *Li and Peng* [2002].

Overall, our confidence in the most appropriate C_{org}:P ratio value is low. Model runs with a disequilibrium term that scales linearly with age suggest that for every 0.1 μmol C_T kg^{-1} decrease in the degree of supersaturation per year, the predicted C_{org}:P ratio decreases by ~5.

We, like *Li and Peng* [2002], find a lower $-O_2$:P ratio than was found by several recent studies [*Broecker et al.,* 1985; *Takahashi et al.,* 1985; *Anderson and Sarmiento* 1994; *Körtzinger et al.,* 2001]. Regional differences may account for this low observation since these other studies mostly avoided the Southern Ocean. *Li and Peng* [*2002*] find regional variability in the $-O_2$:P ratio and indicate a maximum value of 162

found in the Northern Pacific. They attribute the higher North Pacific $-O_2$:P ratio to differences in the average oxidation state of the degrading organic matter. However, *Li and Peng* [2002] also argue that high $-O_2$:P ratio estimates in other studies are the result of an underestimation of the number of endmembers mixing in the water masses considered or complications with how endmembers are defined. While direct comparison with other regions using this model is impossible, we demonstrate that neglecting mixing entirely yields higher $-O_2$:P ratios for the isopycnals that outcrop in this region using two simple analyses: a direct fit of phosphate and oxygen concentrations interpolated along the 27.1 σ_Θ isopycnal using the GLODAP dataset [*Key et al.*, 2004] from 58 ºS to 15 ºS along CLIVAR leg P18 yields the substantially higher $-O_2$:P ratio of 184. This same data yields a $-O_2$:P ratio of 145 when along-isopycnal mixing is accounted for using a 2-endmember mixing approach.

The influence of diapycnal mixing on Redfield ratios is understood in the context of the diffusion of PO [*Broecker*, 1974]: the mean value of the second derivative of this tracer in the GLODAP dataset goes from negative near the surface to positive at intermediate depths whether calculated with an $-O_2$:P ratio of 131 or 170. This indicates a net diffusive gain of this tracer near the ocean's surface and a net loss near oxygen minimum zones. Estimated $-O_2$:P ratios that neglect diapycnal mixing, if a significant amount is present, would therefore require increased phosphate-dominated PO contributions at depth relative to the oxygen-dominated contributions near the surface, and would shift the $-O_2$:P ratio to counter this unaccounted-for upwards diffusion of PO.

2.4.5 Coastal influences

Table 2.4 Process rates, Redfield ratios, and confidence intervals for subdivided datasets.

Term	Units	Off-shore (>80 °W)			Near-shore (<80 °W)		
		Value	± (95%)	N	Value	± (95%)	N
s rate (mix)	$\mu mol\ kg^{-1}\ yr^{-1}$	0.016	0.001	66	0.024	0.003	18
h rate (mix)	$\mu mol\ kg^{-1}\ yr^{-1}$	0.16	0.02	66	0.10	0.02	18
$R_{N:P}$	-	16.4	0.8	77	14.2	0.7	22
$R_{-O2:P}$	-	131	6	77	131	8	22
$R_{Corg:P}$ (mix)	-	126	6	77	99	7	22

Model outputs estimated using only data obtained west and east of 80° W are presented in Table 2.4. Differences between these sets of model outputs suggest that sedimentary remineralization and landmass runoff are potentially significant sources of bias for the overall model output estimates. Near shore data indicate a higher soft tissue pump rate, a lower hard tissue pump rate, a lower $R_{N:P}$, and a lower $R_{C:P}$ than either the offshore data or the undivided data. While these observations are consistent with the possibility of near-shore freshwater runoff, high rates of sedimentary organic matter remineralization, and sedimentary denitrification, it is impossible to assign cause with any certainty. It is possible that the outputs obtained using the offshore data are indeed better estimates for open-ocean processes, though adopting them would not significantly affect our conclusions.

2.4.6 Preformed gas saturations

An added complication for model outputs involving the oxygen and C_T is that the degree of saturation of the DML component over time might not be constant for these properties. However, a regression of the residuals of the fits of equations 24 and 25 against mixing age yields no statistically significant trend for C_T or O_2 over time. This implies that either there are no resolvable long term linear trends in these gases' initial

saturations or that any trend present is too highly covariant with the increase in nutrient concentrations with water parcel age to distinguish.

Also of interest is to what degree apparent preformed gas disequilibria are due to actual disequilibria in subducting surface waters versus to subsurface mixing. The deep mixed layers characterized in this study are 97.4% saturated with respect to atmospheric oxygen, but only 0.03% supersaturated with respect to C_T (0.5 μmol kg^{-1} excess), and ~97% saturated with respect to CFC-11 and CFC-12. By contrast, the preformed oxygen saturation analysis used by *Russell and Dickson* [2003] suggests that AAIW is ~85% saturated with respect to oxygen at formation. *Russell and Dickson* [2003] back-estimate initial nutrient concentrations of 24 μmol NO_3^- kg^{-1} and 1.67 μmol PO_4^{3-} kg^{-1}. Deep mixed layer component measurements have only 20.5 μmol NO_3^- kg^{-1} and 1.46 μmol PO_4^{3-} kg^{-1}. These observations can be collectively explained by vigorous subsurface mixing during entrainment of deep mixed layer water into the SAMW and AAIW masses. For example, a mixture of 39% UCDW and 61% DML component would be expected to have 24 μmol NO_3^- kg^{-1}, 1.68 μmol PO_4^{3-} kg^{-1}, a salinity of 34.21, a potential temperature of 4.81 ºC, and 268 μmol O_2 kg^{-1}. This corresponds to 86% oxygen saturation. Waters with similar oxygen, nitrate, and phosphate concentrations are found just below and to the North of the deep mixed layers in the AAIW2005 dataset.

The assumption that the deep mixed layers measured are representative of the mixed layer water that is ultimately entrained into intermediate and mode waters allows the determination of an initial ΔC^*_{diseq} for this subducting water. Using ΔC^*_{diseq} formulas given by *Sabine et al.* [2002] with the Redfield ratios published by *Anderson and Sarmiento* [1994], treating the DML component as a subducting water mass with an age

of 0 years, and using the measured alkalinity in place of the TA° term for the equilibrium alkalinity, we estimate a ΔC^*_{diseq} of 2.2 µmol C* kg^{-1} for this DML component. If, as is typically done using ΔC^*, the TA° is used as the equilibrium alkalinity and the traditional CFC age is estimated from the measured DML CFC concentrations, the ΔC_{diseq} estimate becomes –8.8 µmol C* kg^{-1}.   For comparison, we also use our mixing model to simulate the most relevant endmember detailed by *Sabine et al.* [2002]. Endmember 2e in this paper has several characteristics indicative of AAIW including a high oxygen concentration (281 µmol O$_2$ kg^{-1}), an intermediate potential temperature (5.31 ºC), a low salinity (34.220), and an appropriate outcropping latitude (54 °S). This salinity and potential temperature is consistent with a DML : SSW : UCDW mixing ratio of 47 : 38 : 15. We use this mixing ratio to obtain a property distribution for this mixture, and then use this property distribution to estimate a ΔC^*_{diseq} term. The associated phosphate and nitrate concentrations agree with the endmember concentrations published in *Sabine et al.* [2002] to within 0.03 and 0.2 µmol kg^{-1} respectively. The ΔC^*_{diseq} estimate of –5.6 µmol C* kg^{-1} is lower than the ΔC^*_{diseq} estimate obtained by *Sabine et al.* [2002] (-7.4 µmol C* kg^{-1}), but the disagreement is small relative to the minimum uncertainty inherent the ΔC^*_{diseq} term (± 5 µmol C* kg^{-1}). This independent estimate of the disequilibrium term for AAIW lends credence to the ΔC^* technique's assumption that this term is constant over time for this water mass to within the estimated uncertainties. Inferring more information from this comparison is impossible given possible discrepancies in the CFC dating methods used. For example, if this hypothetical mixture is attributed a 0 age (instead of inferring a traditional CFC age from the mixture's CFC concentrations), the disequilibrium term becomes -16.1 µmol C* kg^{-1}.

2.5 Summary and Conclusions

We argue both that vigorous initial and subsequent mixing is responsible for setting the properties of SAMW and AAIW and that many commonly used biogeochemical estimates stand to benefit from further parameterizations for mixing. We describe a unique hydrographic dataset collected in the Southern Ocean in the season of deep mixed layer, AAIW, and SAMW formation, and we use this dataset to construct a novel three-component inverse mixing model with a subducting surface component. The model parameterizes for the effects of mixing, biology, gas exchange with an evolving atmosphere, and secular warming and freshening. We introduce a CFC dating method that is specialized for estimating the age of a single component in a mixture of waters. We apply this model to the entrainment of deep wintertime mixed layer waters into the AAIW and SAMW masses.

Mixing ratios suggest that DML entrainment reaches a subsurface maximum that fits well with the assumed mixing patterns. While the exact depth of the DML component maximum is dependent upon model assumptions, the model indicates substantial contributions of deep mixed layer water to both the potential vorticity minimum region characteristic of SAMW and to the salinity minimum region characteristic of AAIW.

Our model yields a calcium carbonate dissolution rate estimate that is roughly half the estimate obtained using the TA* method for the Southern Ocean. A change in assumed shallow calcium carbonate dissolution flux should have consequences for estimates of global carbonate export fluxes [*Berelson et al.,* 2007]. Given the

uncertainties in TA* resulting from mixing and the method by which preformed potential alkalinity is estimated, we conclude that TA* is best used as a global tracer for calcium carbonate dissolution rather than as a local or regional tracer. Our estimates of shallow calcium carbonate dissolution rate are still statistically distinguishable from zero however, and shallow depth calcium carbonate dissolution is still thought to be significant process in the Southern Ocean.

Our estimates for Redfield ratios for this region are in good agreement with the ratios obtained by *Li and Peng* [2002] with the exception of the C_{org}:P ratio. We conclude that the C_{org}:P ratio in *Li and Peng* [2002] is underestimated for this region due to a lack of a parameterization for anthropogenic carbon uptake. We obtain a $-O_2$:P ratio of 135 that is substantially lower than many recent estimates for other regions, but in agreement with *Li and Peng* [2002]. It is unclear whether low $-O_2$:P ratios are the result of differences in how the effects of mixing are estimated or reflect a regional difference.

We show that recent estimates of initial AAIW oxygen and ΔC^* atmospheric disequilibria are attributable to the effects of subsurface mixing during entrainment rather than a direct air-sea disequilibrium in the AAIW formation region. Deep mixed layer water oxygen concentrations are found to be 97.4% of saturation and ΔC^*_{diseq} values are estimated at 2.2 μmol kg^{-1}. We determine the ΔC^*_{diseq} value of the endmember given by *Sabine et al.* [2002] that most closely resembles AAIW using our mixing model and find no evidence to suggest this value is changing for this water mass beyond the ΔC^* technique's minimum uncertainty of ± 5 μmol kg^{-1}.

The mixing model and CFC mixing age technique introduced herein are likely to be useful only in regions where there is reason to believe that a well-characterized surface

water mass is a dominant component of a subsurface water mass. The model's application is therefore limited in scope until more data collection efforts have characterized water in deep water formation regions in the season in which the deep water is forming.

2.6 Acknowledgements

2.7 Chapter 2 Appendix

This section demonstrates that it is not necessary to define a mixing trend using "pure" endmember water masses that are free of the component of interest provided the stated assumptions hold. This can be shown straightforwardly for the simpler case of two-endmember mixing. Assuming for the moment that the mixing trend is defined

between a pure DML component and a totally DML-free component, a change in a

property "X" resulting from a process acting upon the DML component would be solved

for using:

$$X = X_1(1-f_2) + X_2 f_2 + \Delta X(1-f_2) \tag{26}$$

$$\Delta X = \frac{X - X_1(1-f_2) - X_2 f_2}{(1-f_2)} \tag{27}$$

Here the subscript 1 refers to the DML component and the subscript 2 to the DML-free

endmember component. We now compare this result to the solution to the more complex

case in which the property distribution of the non-DML component is defined using data

from water that does contain a portion of DML waters. We first derive the value of

property X expected for this mixture:

$$X_M = X_1(1-f_M) + X_2 f_M + \Delta X(1-f_M) \tag{28}$$

Here, f_M represents the fraction of the mixed component that originated from the pure

DML-free endmember. Substituting this mixture property value into equation (27) in

place of X_2 and using f_D to refer to the new mixing fraction estimate that would be

obtained with the mixture's property distribution, we obtain:

$$\Delta X = \frac{X - X_1(1-f_D) - X_1(1-f_M)f_D - X_2 f_M f_D - \Delta X(1-f_M)f_D}{(1-f_D)} \tag{29}$$

This can be simplified to:

$$\Delta X = \frac{X - X_1(1-f_M f_D) - X_2 f_M f_D}{(1-f_M f_D)} \tag{30}$$

It can also be straightforwardly shown for this case that:

$$f_M f_D = f_2 \qquad (31)$$

and therefore that both estimates of the change in the property X resulting from the process are equal. This can also be shown to apply to the three-component mixing case numerically.

References for Chapter 2

Anderson, L. A. (1995), On the hydrogen and oxygen content of marine phytoplankton, *Deep Sea Research Part I: Oceanographic Research Papers, 42*, 1675-1680.

Anderson, L. A. and J. L. Sarmiento (1994), Redfield ratios of remineralization determined by nutrient data analysis, *Global Biogeochem. Cycles, 8*, 65-80.

Anderson, L. A. and J. L. Sarmiento (1995), Global ocean phosphate and oxygen simulations, *Global Biogeochem. Cycles, 9*, 621-636.

Berelson, W. M., W. M. Balch, R. Najjar, R. A. Feely, C. Sabine, and K. Lee (2007), Relating estimates of $CaCO_3$ production, export, and dissolution in the water column to measurements of $CaCO_3$ rain into sediment traps and dissolution on the sea floor: A revised global carbonate budget, *Global Biogeochem. Cycles, 21*, GB1024.

Böning, C. W., A. Dispert, M. Visbeck, S. R. Rintoul, and F. U. Schwarzkopf (2008), The response of the Antarctic Circumpolar Current to recent climate change, *Nature Geoscience, 1*, 864-869.

Brewer, P. G. and J. C. Goldman (1976), Alkalinity changes generated by phytoplankton growth, *Limnol. Oceanogr., 21*, 108-117.

Broecker, W. S. (1974), NO, a conservative water-mass tracer, *Earth Planet. Sci. Lett., 23*, 100-107.

Buesseler, K. O. (1991), Do upper-ocean sediment traps provide an accurate record of particle flux?, *Nature, 353*, 420-423.

Dickson, A. G. (1990), Thermodynamics of the dissociation of boric acid in synthetic seawater from 273.15 to 318.15 K, *Deep Sea Research Part A.Oceanographic Research Papers, 37*, 755-766.

Dickson, A. G. and F. J. Millero (1987), A comparison of the equilibrium constants for the dissociation of carbonic acid in seawater media, *Deep Sea Research Part A.Oceanographic Research Papers, 34*, 1733-1743.

Feely, R. A., C. L. Sabine, K. Lee, W. Berelson, J. Kleypas, V. J. Fabry, and F. J. Millero (2004), Impact of anthropogenic CO_2 on the $CaCO_3$ system in the oceans, *Science, 305*, 362.

Feely, R. A., C. L. Sabine, K. Lee, F. J. Millero, M. F. Lamb, D. Greeley, J. L. Bullister, R. M. Key, T. H. Peng, and A. Kozyr (2002), In situ calcium carbonate dissolution in the Pacific Ocean, *Global Biogeochem. Cycles, 16*, 1144.

Fine, R. A. (1993), Circulation of Antarctic intermediate water in the South Indian Ocean*, Deep Sea Research Part I: Oceanographic Research Papers, 40*, 2021-2042.

Friis, K., R. G. Najjar, M. J. Follows, and S. Dutkiewicz (2006), Possible overestimation of shallow-depth calcium carbonate dissolution in the ocean*, Global Biogeochem. Cycles, 20*, GB4019.

Friis, K., R. G. Najjar, M. J. Follows, S. Dutkiewicz, A. Körtzinger, and K. M. Johnson (2007), Dissolution of calcium carbonate: observations and model results in the subpolar North Atlantic*, Biogeosciences, 4*, 205-213.

Garcia, H. E. and L. I. Gordon (1992), Oxygen solubility in seawater: Better fitting equations*, Limnol. Oceanogr.*, 1307-1312.

Gruber, N. and J. L. Sarmiento (1997), Global patterns of marine nitrogen fixation and denitrification*, Global Biogeochem. Cycles, 11*, 235-266.

Gruber, N., J. L. Sarmiento, and T. F. Stocker (1996), An improved method for detecting anthropogenic CO_2 in the oceans*, Global Biogeochem. Cycles, 10*, 809-837.

Hedges, J. I., J. A. Baldock, Y. Gelinas, C. Lee, M. L. Peterson, and S. G. Wakeham (2002), The biochemical and elemental compositions of marine plankton: A NMR perspective*, Mar. Chem., 78*, 47-63.

Honjo, S., R. Francois, S. Manganini, J. Dymond, and R. Collier (2000), Particle fluxes to the interior of the Southern Ocean in the Western Pacific sector along 170 W*, Deep Sea Research Part II: Topical Studies in Oceanography, 47*, 3521-3548.

Jackett, D. R. and T. J. McDougall (1997), A neutral density variable for the world's oceans*, J. Phys. Oceanogr., 27*, 237-263.

Kanamori, S. and H. Ikegami (1982), Calcium-alkalinity relationship in the North Pacific*, J. Oceanogr., 38*, 57-62.

Karsten, R., H. Jones, and J. Marshall (2002), The role of eddy transfer in setting the stratification and transport of a circumpolar current*, J. Phys. Oceanogr., 32*, 39-54.

Key, R. M., A. Kozyr, C. L. Sabine, K. Lee, R. Wanninkhof, J. L. Bullister, R. A. Feely, F. J. Millero, C. Mordy, and T. H. Peng (2004), A global ocean carbon climatology: Results from Global Data Analysis Project (GLODAP)*, Global Biogeochem. Cycles, 18*, GB4031.

Kortzinger, A., J. I. Hedges, and P. D. Quay (2001), Redfield ratios revisited: Removing the biasing effect of anthropogenic CO_2*, Limnol. Oceanogr.*, 964-970.

Lenton, A. and R. J. Matear (2007), Role of the Southern Annular Mode (SAM) in Southern Ocean CO_2 uptake, *Global Biogeochem. Cycles, 21*, GB2016.

Li, Y. H. and T. H. Peng (2002), Latitudinal change of remineralization ratios in the oceans and its implication for nutrient cycles, *Global Biogeochem. Cycles, 16*, 1130.

Lovenduski, N. S., N. Gruber, S. C. Doney, and I. D. Lima (2007), Enhanced CO_2 outgassing in the Southern Ocean from a positive phase of the Southern Annular Mode, *Global Biogeochem. Cycles, 21*, GB2026.

Macdonald, A. M. (1993), Property fluxes at 30° S and their implications for the Pacific-Indian throughflow and the global heat budget, *Journal of Geophysical Research, 98*, 6851-6868.

Martin, J. H., R. M. Gordon, S. Fitzwater, and W. W. Broenkow (1989), VERTEX: phytoplankton/iron studies in the Gulf of Alaska, *Deep Sea Research Part A.Oceanographic Research Papers, 36*, 649-680.

McCartney, M. S. (1979), *Subantarctic Mode Water*, Woods Hole Oceanographic Institution.

Mecking, S., M. J. Warner, C. E. Greene, S. L. Hautala, and R. E. Sonnerup (2004), Influence of mixing on CFC uptake and CFC ages in the North Pacific thermocline, C07014.

Mehrbach, C., C. H. Culberson, J. E. Hawley, and R. M. Pytkowicz (1973), Measurement of the apparent dissociation constants of carbonic acid in seawater at atmospheric pressure, *Limnol. Oceanogr., 18*, 897-907.

Redfield, A. C., B. H. Ketchum, and F. A. Richards (1963), The influence of organisms on the composition of sea-water, 26-77.

Russell, J. L. and A. G. Dickson (2003), Variability in oxygen and nutrients in South Pacific Antarctic Intermediate Water, *Global Biogeochem. Cycles, 17*, 1033.

Sabine, C. L., R. A. Feely, N. Gruber, R. M. Key, K. Lee, J. L. Bullister, R. Wanninkhof, C. S. Wong, D. W. R. Wallace, and B. Tilbrook (2004), The oceanic sink for anthropogenic CO_2, *Science, 305*, 367-371.

Sarmiento, J. L., G. Thiele, R. M. Key, and W. S. Moore (1990), Oxygen and nitrate new production and remineralization in the North Atlantic subtropical gyre, *J.Geophys.Res, 95*, 18,315.

Sloyan, B. M. and S. R. Rintoul (2001), The Southern Ocean Limb of the Global Deep Overturning Circulation, 143-173.

Sloyan, B. M., L. D. Talley, T. K. Chereskin, R. Fine, and J. Holte (2010), Antarctic Intermediate Water and Subantarctic Mode Water Formation in the southeast Pacific: the role of turbulent mixing, *J. Phys. Oceanogr.*, DOI: 10.1175/2010JPO4114.

Sonnerup, R. E. (2001), On the relations among CFC derived water mass ages, *Geophys. Res. Lett., 28*, 1739-1742.

Stommel, H. (1979), Determination of water mass properties of water pumped down from the Ekman layer to the geostrophic flow below, *Proc. Natl. Acad. Sci. U. S. A., 76*, 3051.

Takahashi, T., W. S. Broecker, and S. Langer (1985), Redfield ratio based on chemical data from isopycnal surfaces, *Journal of Geophysical Research, 90*, 6907-6924.

Trull, T. W., S. G. Bray, S. J. Manganini, S. Honjo, and R. Francois (2001), Moored sediment trap measurements of carbon export in the Subantarctic and Polar Frontal Zones of the Southern Ocean, south of Australia, *Journal of Geophysical Research, 106*, 31489.

van Heuven, S., D. Pierrot, E. Lewis, and D. Wallace (2009), MATLAB Program developed for CO_2 system calculations, *ORNL/CDIAC-105b, Carbon Dioxide Information Analysis Center, Oak Ridge National Laboratory, US Department of Energy, Oak Ridge, Tennessee*.

Warner, M. J. and R. F. Weiss (1985), Solubilities of chlorofluorocarbons 11 and 12 in water and seawater, *Deep Sea Research Part A.Oceanographic Research Papers, 32*, 1485-1497.

Wong, A. P. S., N. L. Bindoff, and J. A. Church (2001), Freshwater and heat changes in the North and South Pacific Oceans between the 1960s and 1985–94.

Yu, E. F., R. Francois, M. P. Bacon, S. Honjo, A. P. Fleer, S. J. Manganini, M. M. van der Loeff, and V. Ittekot (2001), Trapping efficiency of bottom-tethered sediment traps estimated from the intercepted fluxes of 230Th and 231Pa, *Deep Sea Research Part I: Oceanographic Research Papers, 48*, 865-889.

Chapter 3: Inferring changes in biogeochemical processes from hydrographic property measurements in the Pacific sector of the Southern Ocean

3.1 Abstract

Observations and models suggest that the Southern Ocean is especially sensitive to climate change. We compare two pairs of recent hydrographic records collected more than a decade apart to determine whether these datasets are consistent with a continuation of observed and projected trends. We also present and employ an inverse model that estimates changes in the relative strengths of processes from differences in measurements of physical properties, nutrient concentrations, and carbonate system parameters. Model results and data comparisons indicate long term warming and freshening trends in the intermediate and mode water masses forming in the Southeastern Pacific that are consistent with other published estimates. Additionally, we observe a strong steepening of isopycnals across the Antarctic Circumpolar Current consistent with an increase in upwelling from increased Ekman divergence associated with intensifying westerlies. A sensitivity analysis suggests that this model stands to benefit substantially from improvements in the analytical confidence of the modeled property measurements.

3.2 Introduction

The atmospheric and oceanic reservoirs near Antarctica are increasingly recognized as hotspots of global climate change. Researchers have used observations and inverse models to provide evidence for long-term changes in freshwater and heat budgets,

circulation patterns, and the balance of gas transfer between the atmosphere and the ocean in this region [*Johnson and Orsi*, 1997; *Thompson and Solomon*, 2002; *Aoki et al.*, 2005; *LeQuéré et al.*, 2007; *Böning et al.*, 2008]. Additionally, numerous hind-cast and forecast global circulation model (GCM) studies have explored the mechanisms of these changes and predicted how they will respond to the likely climate forcing of the future [*Sarmiento et al.*, 1998; *Banks and Bindoff*, 2002; *Gnanadesikan et al.*, 2007; *Lovenduski et al.*, 2007, 2008; *Downes et al.*, 2009]. In this study we employ results from the Climate Variability (CLIVAR) and World Ocean Circulation Experiment (WOCE) data collection efforts to examine whether these past and predicted trends in the Southern Ocean fit with decadal variability in recent hydrographic property records in the Southern Pacific. In this section, we briefly characterize the dominant circulation patterns of the Southern Ocean, discuss the significance of this region for global climate, summarize recent findings regarding long term changes near Antarctica, and outline our basic approach.

Circulation patterns of the Southern Ocean—The intense westerly winds of the Southern Polar Vortex and the lack of continental obstructions along entire lines of latitude of the Southern Ocean give rise to the steeply-sloping isopycnals of the swift and deep Antarctic Circumpolar Current (ACC). Strong Ekman divergence from gradients in these westerlies leads to the upwelling of Upper Circumpolar Deep Water (UCDW) near the Polar Front (PF) [*Speer et al.*, 2000]. This upwelling of deeper waters is balanced by northward Ekman advection of surface waters across the ACC and into the region of Antarctic Intermediate Water (AAIW) and Subantarctic Mode Water (SAMW) formation. These thermocline water masses are thought to originate from the

incorporation of deep wintertime mixed layers found between the Subtropical Front

(STF) and the Subantarctic Front (SAF). The deepest, densest, and furthest south of

these mixed layers are found in the Southeastern Pacific, and this region is thought to be

a hotspot for the formation of AAIW and SAMW [*Sloyan and Rintoul*, 2000]. However,

attempts to account for movement of water in the ACC and the density structure in the

region have suggested that at least a portion of the northward surface transport must also

be counteracted by a strong eddy return flux [*Speer et al.*, 2000; *Böning et al*, 2008].

Significance of the region—These circulation patterns collectively make the

Southern Ocean a central piece of both the upward and downward limbs of the global

overturning circulation, and hence a crucial region for the ventilation of the ocean. The

AAIW mass has been estimated to contain $1/6^{th}$ of the ocean's total anthropogenic CO_2

inventory [*Sabine et al.*, 2004] and represent a significant fraction of the interannual

variability in its uptake [*Lenton and Matear*, 2007; *Lovenduski et al.*, 2007]. It also

introduces a large amount of oxygen into the ocean interior [*Russell and Dickson*, 2003].

In addition, the upwelling of UCDW maintains one of the largest areas of consistently

high surface ocean nutrient concentrations in the ocean.

Long term trends in the Southern Ocean— It is generally accepted that there has

been a long term increase in the Southern Annular Mode index (SAM), or the pressure

gradient between the mid-latitudes and the South Pole, since the late 1970's [*Thompson*

and Solomon, 2002]. This corresponds to an increase in the intensity of the westerlies

over the Southern Ocean that some GCMs suggest will intensify the overturning

circulation of the ACC. *LeQuéré et al.* [2007] use an atmospheric inversion to

demonstrate that this trend has led to a decrease in the efficiency of the Southern Ocean

carbon dioxide sink since 1981 through increased degassing of high $p(CO_2)$ UCDW. This finding has been both supported [*LeQuéré et al.*, 2008; *Lovenduski et al.*, 2008] and opposed [*Law et al.*, 2008; *Zickfeld et al.*, 2008] by subsequent research. It also remains unclear whether the increase in the northward transport will be balanced by an increase in the formation of intermediate waters, or whether this increase will be prevented by increased stratification resulting from projected warming and freshening trends in the ACC [*Held and Soden*, 2006; *Gnanadesikan et al.*, 2007] or by an compensating increase in the southward eddy return flow [*Böning et al.*, 2008]. *Johnson and Orsi* [1997], *Wong et al.* [2001], *Aoki et al.* [2005], and *Böning et al.* [2008], provide evidence for these projected warming and freshening trends occurring in the ACC through the 1990s using comparisons between hydrographic data in the Indian and Pacific oceans.

Collectively, these studies raise several questions regarding the long term changes in the Pacific sector of the ACC:

(1) Have the trends that have been found continued through the modern day in the Pacific?

(2) Has the increase in the SAM index led to an increase in the upwelling of UCDW?

(3) … or, is there evidence for the Northward advection of upwelled water being offset by an increasing eddy return flux?

(4) Has AAIW formation slowed?

(5) Can, as *Lovenduski et al.* [2008] suggest, oxygen changes be used to shed light on the efficiency of the carbon dioxide sink?

In this chapter we examine differences between two records of two hydrographic sections (P16S and P18S), each occupied once during the early 1990s and again ~14

years later, in an effort to address these questions. The central difficulty of this approach is assigning causes to observed changes in property measurements when there are typically multiple processes at work (such as warming, freshening, and heaving or deepening of water masses). The traditional approach of processing large quantities of data collected at a range of times to average out vertical water mass displacements is impossible with only two records. Instead, we employ an optimum multiparameter (OMP) model that relies upon differences in salinity, potential temperature, and 6 other measured properties to deconvolute the effects of changes in the various processes.

3.3 Methods

For the reasons *Wong et al.* [2001] recommend, we consider differences found along both surfaces of constant depth (referred to here as isobars) and surfaces of constant density (isopycnals). Our approach to estimating the differences between these records is straightforward:

(1) We interpolate the individual measurements onto evenly-spaced grids of latitude and depth and of latitude and neutral density to allow direct comparison between records.

(2) We subtract the interpolated older datasets from the interpolated recent datasets.

(3) We present and discuss the differences in a qualitative manner.

(4) We employ an optimum multiparameter (OMP) inverse model to objectively estimate changes in various processes and discuss the results.

In this section we detail the datasets used, how our interpolations are accomplished, and how the inverse model estimates process changes. This section

concludes with an estimation of the uncertainty in the property differences and the model

outputs from uncertainties in the data and in the model assumptions.
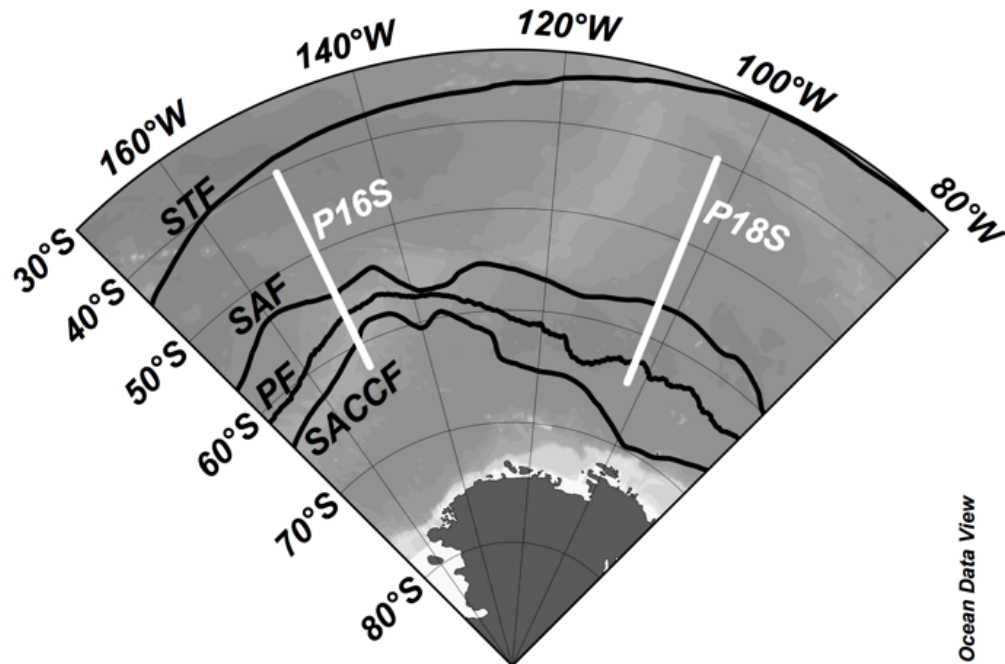
Figure 3.1 A map indicating the locations of the two sections considered, P16 and P18, as white lines and the average locations of the Southern Ocean's various fronts as given by *Orsi et al.* [1995] as black lines.

Datasets used—Both of the P16S and the P18S datasets were collected along the

tracks shown in Figure 3.1. The dates of the cruises, the meridians occupied, and the

lengths of time elapsed between the pairs of occupations are given in Table 3.1. The two

initial datasets collected as part of the WOCE program are extracted from the Global

Ocean Data Analysis Project (GLODAP) bottle dataset. *Key et al.* [2004] have

undergone an extensive process of quality controlling these measurements using data

collected at depth along repeat occupations of individual stations. Any data from any

dataset not flagged as either "good" or the "average of replicate measurements"(QC

codes 2 and 6) is discarded prior to interpolation. The properties considered are potential

temperature (Θ), salinity (S), dissolved oxygen ($[O_2]$), total silicate ($[Si(OH)_4]$), total

phosphate ($[PO_4^{3-}]$), nitrate ($[NO_3^-]$), total alkalinity (A_T), total dissolved inorganic

carbon (C_T), neutral density (γ_n: determined using the formulation of *Jacket and*

McDougall [1997]), and depth (z).

Table 3.1 Dates and meridians of the data collection cruises. Front locations from *Orsi et al.* [1995] are provided for the meridians indicated.

Section	1st occupation (19yy−mm−dd)	2nd occupation (20yy−mm−dd)	Date Δ (y)	Long (°E)	STF (°S)	SAF (°S)	PF (°S)	SACCF (°S)
P16S	91/07/16 – 91/08/25	05/01/09 – 05/02/19	13.5	−150	38.0	54.7	57.0	59.5
P18S	94/01/26 – 94/04/27	07/12/15 – 08/02/23	13.8	−103	30.7	56.9	62.6	68.4

Interpolation method—Data are interpolated along a grid of fixed latitude, depth,

and density intervals that span 30 to 70 °S with 1/4° spacing, 0 to 4000 m depth with 50

m spacing, and 26.3 to 28.3 kg m^{-3} with 0.025 kg m^{-3} spacing. The interpolation scheme

employed is similar, though not identical, to the procedure described by *Key et al.* [2004].

Interpolation is accomplished in four steps:

1. For each station, data is interpolated vertically onto the grid's depth and density surfaces using the Matlab piecewise cubic Hermite interpolating polynomial function.

2. Extrapolations and any interpolations made between data points that are more than $100 + z/10$ meters (where z is the depth of the interpolated data) away from the interpolation depth or more than 0.1 kg m^{-3} away from the interpolation density are discarded.

3. Interpolations at a given depth are then linearly interpolated onto the grid's latitude intervals.

4. Step 2 is repeated for the latitude interpolation with a distance limit of 1 ° of latitude.

5. Steps 1 through 4 are repeated for both records of both sections (4 times in total).

We have found that this interpolation scheme yields gridded property fields (and differences between property fields) that are similar to results from an alternate interpolation method: Delaunay Triangulation with 1 ° of latitude separation weighted to be equivalent to 100 m depth separation and 0.3 kg m^{-3}.

After obtaining the interpolated datasets, the differences in the gridded properties are determined by subtracting the older dataset from the more recent dataset:

$$D = I_{CLIVAR} - I_{GLODAP} \tag{1}$$

Here I represents the interpolated datasets and D is a matrix of differences between the 8 property measurements interpolated at each latitude and depth coordinate.

We discuss patterns of differences within the top 1000 meters. Several regions of the depth and density ranges considered show distinct patterns of property differences. We consider average differences and model outputs for the regions indicated in Figure 3.2. The main feature that divides these regions is the SAF. Region G is the approximate depth region of the SAMW mass, and region H represents the lowest reaches of the AAIW mass.
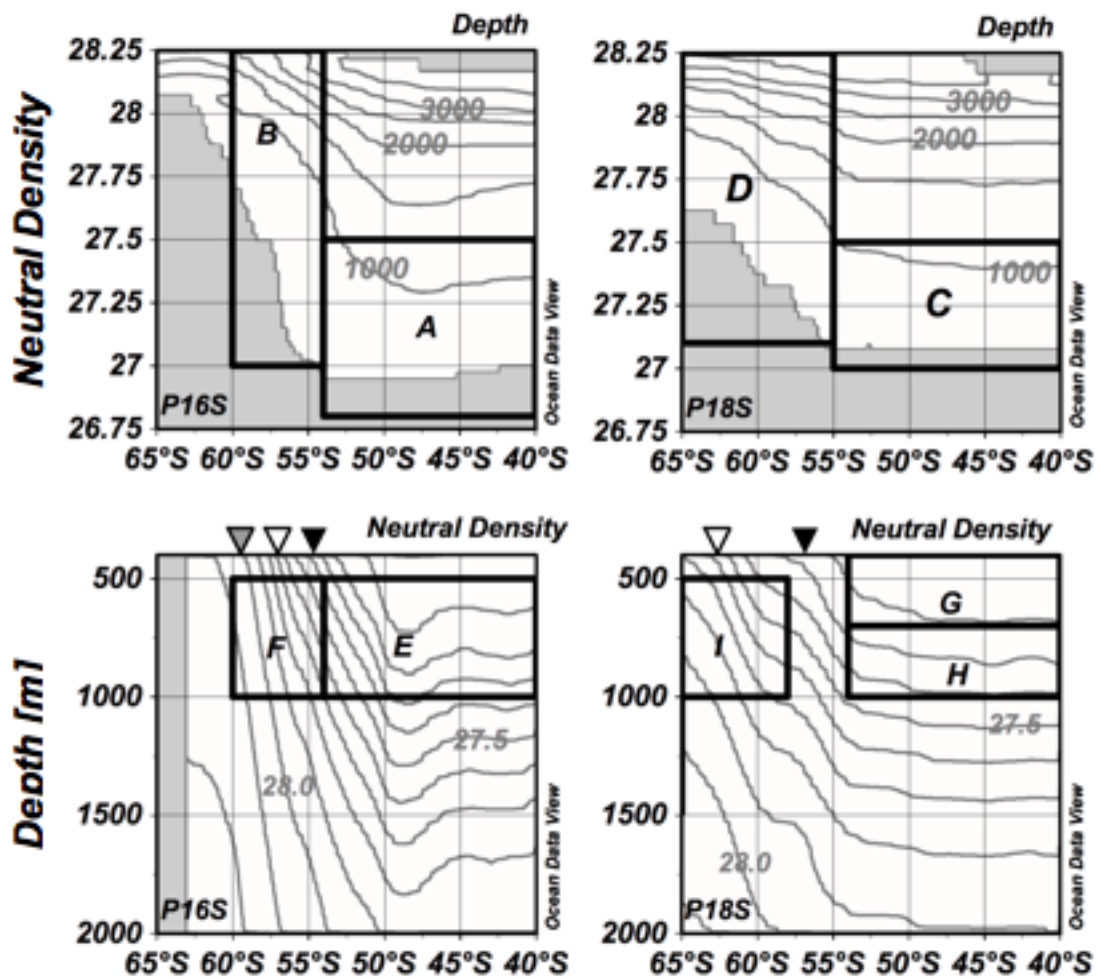
Figure 3.2 Figures indicating the locations of isobars in density space (top) and isopycnals in space (bottom) in the earlier datasets collected along the P16S (left) and P18S (right) sections. Triangles mark the average latitude of SAF (black), PF (white), and SACCF (grey) fronts at the ocean's surface. Regions enclosed by grey rectangles are regions of interest that are referred to by letter in the discussion. Data with an interpolated depth less than 500 m is not displayed in the top two figures or included in the density regions.

Possible problems originating from cruise-to-cruise measurement biases are partially addressed by assuming that there are no decadal changes in the water found between 3000 and 4000 m depth. We apply a linear adjustment to all properties wherein the average interpolated property differences over this depth range are subtracted from all differences for that section regardless of depth. The values of these adjustments are

provided in Table 3.2. The possibility that this adjustment is inappropriate for all or some of the data is considered in the error assessment section.

Table 3.2 Average property differences found for data interpolated between 3000 and 4000 m depth.

Section	Θ (°C)	S	$[NO_3^-]$*	$[PO_3^-]$*	A_T*	$[Si(OH)_4]$*	$[O_2]$*	C_T*
P16S	0.003	0.0002	0.07	0.001	0.4	−0.27	−1.4	2.2
P18S	0.011	0.0025	0.74	0.009	1.8	0.73	−1.8	0.6

* units are μmol kg^{-1}

The OMP model— An OMP inverse model is used to aid in the interpretation of the differences between the datasets interpolated along isobars between 400 and 1000 m depth. This depth range is targeted because it is thought to be shallow enough to have the potential for decadal variability, but deep enough to not be affected by seasonal or shorter time-scale processes.

The model optimizes 6 terms for each set of interpolated property differences. Each term allows water properties to change by a different process. The processes (and their associated terms) are vertical displacement of water parcels (Δz), an increase or decrease in the activity of the soft and hard tissue pumps (Δbio), the addition or removal of freshwater (Δf), warming or cooling (Δh), and net oxygen and C_T exchange with the atmosphere (ΔgO and ΔgC respectively). The effects of a change in these processes are expressed as "vectors" that relate how the various measured properties should change in response to changes in these processes.

The vertical displacement term reflects shoaling or deepening of water masses due to transient eddies, shifts in the locations of fronts, or other circulation changes. We allow for these changes using a term that perturbs properties along a vector defined by

the gradient of the interpolated properties with respect to density at that location. These slopes are estimated using regressions of each property against density in a dataset comprised of the averages of the interpolated earlier and later datasets. The regressions are fitted using only the data from interpolations at that latitude that indicate a density that is within 0.05 kg m^{-3} of the interpolated water parcel's density. The elements of this process vector are then the individual slopes of these regressions. Using this formulation, the effects of this term are scaled by neutral density such that a Δz value of 1 indicates a density increase of 1 kg m^{-3} resulting from changes in mixing processes.

A term allowing for changes in the soft and hard tissue pumps, Δbio, is necessary to account for the potential for accumulation of the byproducts of the degradation of biological material in a stagnating water mass or the lack of accumulation in a water mass that is overturning more rapidly. We construct such a term from estimates of the rates of activity of the soft and hard tissue pumps in this region determined in chapter 2. We treat both the soft and hard tissue pumps as a single process acting at the rates found in the previous chapter. The net rate of change of a property as a result of biological activity acting over a longer time is then expressed as a function of the Redfield ratio and these rates:

$$
\begin{bmatrix} r_P \\ r_N \\ r_{O2} \\ r_C \\ r_A \\ r_{Si} \end{bmatrix} = \begin{bmatrix} r_S \\ R_{N:P} r_S \\ R_{O2:P} r_S \\ r_H + R_{C:P} r_S \\ 2r_H + R_{A:P} r_S \\ R_{Si:h} r_H \end{bmatrix}
\tag{2}
$$

Here R is the ratio relating changes in the subscripted properties' concentrations and r_S and r_H refer to the rates of the soft and hard tissue pumps expressed in μmol kg^{-1} yr^{-1} of phosphate and carbonate respectively. The Redfield ratios and rates employed are:

$$\begin{bmatrix} R_{N:P} & R_{C:P} & R_{O:P} & R_{A:P} & R_{Si:h} \end{bmatrix} = \begin{bmatrix} 15.2 & 114 & -131 & -16.2 & 1.20 \end{bmatrix} \qquad (3)$$

$$\begin{bmatrix} r_S & r_H \end{bmatrix} = \begin{bmatrix} 0.018 & 0.14 \end{bmatrix} \qquad (4)$$

This vector is therefore normalized to changes in time, and a Δbio model output value of 1 implies an increase in age of 1 year.

The term allowing for changes in the amount of freshwater addition or removal acts to either concentrate or dilute the chemical concentrations already present in the water parcel. This term is normalized to the salinity scale. Changes to other chemical concentrations are then approximated using the ratio of that chemical's concentration to the salinity in the averaged dataset used for the regressions against density. This term only allows for dilution or concentration of existing concentrations, and any heat or gases added or lost with an addition or removal of freshwater are reserved for the Δh, ΔgO, ΔgC terms.

The warming and gas exchange vectors are straightforwardly understood as reflecting changes in the heat budgets or net gas exchange patterns. These vectors are scaled to increase Θ, $[O_2]$, and C_T by a single unit while not changing any other properties. A negative value of these terms indicates cooling or net degassing. Terms with this formulation, that allow one property to vary without changing any other properties, eliminate the usefulness of that property as a constraint for any other process.

Gas concentrations and Θ are therefore included only as benchmarks for change in the activity of these processes and play no role in determining the Δz, Δf, or Δbio terms.

We combine these process term vectors to construct a process matrix, P, with columns referring to individual processes and rows referring to individual properties. For an idealized version of this model, the process matrix would then be multiplied by the changes in these processes, represented here by M, to yield the data:

$$PM \approx D \tag{5}$$

For a given set of interpolation differences the individual elements of P, M, and D are:

$$
\begin{bmatrix}
\Theta_\gamma & 0 & 0 & 1 & 0 & 0 \\
S_\gamma & 0 & 1 & 0 & 0 & 0 \\
[NO_3^-]_\gamma & r_N & [NO_3^-]/S_{avg} & 0 & 0 & 0 \\
[PO_4^{3-}]_\gamma & r_P & [PO_4^{3-}]/S_{avg} & 0 & 0 & 0 \\
A_\gamma & r_A & A_T/S_{avg} & 0 & 0 & 0 \\
[Si(OH)_4]_\gamma & r_{Si} & [Si(OH)_4]/S_{avg} & 0 & 0 & 0 \\
[O_2]_\gamma & r_{O2} & [O_2]/S_{avg} & 0 & 1 & 0 \\
C_\gamma & r_C & C_T/S_{avg} & 0 & 0 & 1
\end{bmatrix}
\begin{bmatrix}
\Delta z \\
\Delta bio \\
\Delta f \\
\Delta h \\
\Delta gO \\
\Delta gC
\end{bmatrix}
\approx
\begin{bmatrix}
\Delta\Theta \\
\Delta S \\
\Delta[NO_3^-] \\
\Delta[PO_4^{3-}] \\
\Delta A \\
\Delta[Si(OH)_4] \\
\Delta[O_2] \\
\Delta C
\end{bmatrix}
\tag{6}
$$

Here, the subscript "γ" indicates that this value is the salinity-normalized slope of that property against density and the subscript "avg" refers to the ratio of those quantities in the averaged dataset at the interpolated location (as described above). The dependency of the elements of P on the location being considered necessitates that each vector of D be considered independently rather than as a matrix of differences.

The equality indicated in equation (5) will not hold for an over-determined system, so instead we optimize this model by minimizing a measure of model misfit. Calculating a single value for model misfit requires that the contributions to model error from each of the constraints be weighted appropriately relative to one another. We

accomplish this in two steps: first, we divide the data and the model parameters by our assessment of the uncertainty of the property measurements themselves. This yields unit-less numbers scaled inversely with the degree of uncertainty in that constraint. The assumed standard deviations of uncertainty used for this are available at the top of Table 3.3. Second, we increase the weight of salinity by a factor of 4 relative to the other properties because its model output is not subject to uncertainties regarding biological processes. As mentioned, the structure of the warming and gas exchange vectors eliminates the importance of the weight for the oxygen, C_T, and Θ parameters.

Model misfit is defined using the L2 norm of the residuals between the data:

$$P_W M - D_W = e \tag{7}$$

$$(P_W M - D_W)^T (P_W M - D_W) = e^T e \tag{8}$$

Here e is the vector of residuals, $e^T e$ is the L2 norm of the residuals, and the subscript W indicates that that data has been weighted as previously indicated. Minimizing the equation for the L2 norm of the residuals with respect to M, the matrix of model outputs, yields the following equation:

$$M_{Min\,L2} = (P_W^T P_W)^{-1} P_W^T D_W \tag{9}$$

$M_{Min\,L2}$ is then the desired output: the vector of process scaling factors that minimizes the misfit of the model to the data. The model outputs are presented as averages over specific regions.

Uncertainty Assessment—Here we provide estimates of interpolation and model output uncertainty obtained by varying inputs and observing how the interpolations and model outputs change.

Table 3.3 Estimated data, data interpolation, and data interpolation difference uncertainties. Uncertainties are expressed as standard deviations.

Dataset	Θ (°C)	S	$[NO_3^-]$*	$[PO_3^-]$*	A_T*	$[Si(OH)_4]$*	$[O_2]$*	C_T*
Input ± (s)	0.0020	0.0020	0.5	0.05	2.0	1.0	1.5	2.0
WOCE interps. ± (s)	0.0024	0.0015	0.4	0.04	1.6	0.9	1.2	1.5
CLIVAR Interps. ± (s)	0.0016	0.0016	0.4	0.04	1.6	0.8	1.2	1.4
Δ Interps. ± (s)	0.0028	0.0021	0.6	0.06	2.1	1.2	1.7	2.1

* units are $\mu mol\ kg^{-1}$

When assessing random data errors, we perturb the data using offsets randomly selected from a population with a mean of 0 and a standard deviation equal to the assumed initial measurement uncertainties. Table 3.3 indicates these assumed uncertainties and the consequent uncertainties in the individual interpolated datasets and in their differences. The effects of random errors in these interpolated differences on the model outputs are assessed by applying offsets from the same population described previously to the interpolated differences. The consequent random errors in the model outputs are given at the top of Table 3.4.

The variability of regional averages of model outputs in response to systematic errors in model inputs is highly dependent upon the property distribution of the region being considered. For each region that we consider, we estimate the variability of model output averages by applying offsets equal to the estimated uncertainties for the model inputs to the data from that specific region. For Redfield ratios, the relative rates of the soft and hard tissue pumps, and each of the fits of the slope of property interpolations against density, we alter the model input to equal the upper 95% confidence interval for the estimate of the value in question. When assessing the model output sensitivity to systematic property input errors, we alter the interpolation differences by a fixed amount

equal to the random uncertainty for that measurement. The results of this sensitivity

analysis are given for region H in Table 3.4.

Table 3.4 Model output sensitivities. *Random*: standard model output deviations (s) resulting from random model input deviations in Table 3.3. *Systematic*: average model output change resulting from the input change indicated. "Property$_\gamma \pm 95\%$" indicates all average changes resulting from variation of each property slope against density added in quadrature.

	Δz	Δbio	Δf	Δh	ΔgO	ΔgC
Random:						
$\pm$ (s) in data	± 0.020	± 2.3	± 0.010	± 0.1	± 5.4	± 4.2
Systematic:						
$\Theta + 0.002$	-	-	-	0.0020	-	-
$S + 0.002$	-0.0004	0.04	0.0021	-0.0023	0.01	-0.15
$[O_2] + 1.5$	-	-	-	-	1.50	-
$[Si(OH)_4] + 1$	0.0112	-1.10	-0.0021	0.0714	-0.31	0.14
$[NO_3^-] + 0.5$	-0.0025	1.53	0.0005	-0.0160	3.09	-2.83
$[PO_4^{3-}] + 0.05$	-0.0014	0.96	0.0002	-0.0087	2.00	-1.84
$C_T + 2$	-	-	-	-	-	2.00
$A_T + 2$	0.0049	-0.67	-0.0008	0.0315	-0.56	0.46
$R_{-O2:P} + 6$	-	-	-	-	0.02	-
$R_{N:P} + 0.6$	-0.0002	0.06	-	-0.0016	0.09	-0.08
$R_{Si:P} + 1$	0.0002	-0.04	-	0.0014	-0.06	0.05
$R_{C:P} + 5$	-	-	-	-	-	0.02
$r_H + 0.1$	-0.0004	0.10	-	-0.0029	0.14	-0.13
Property$_\gamma \pm 95\%$	± 0.0033	± 0.61	± 0.0031	± 0.0298	± 1.41	± 1.17

We also determine 95% confidence intervals for each of the regional property

difference and regional model output averages. These are obtained using the (idealized)

assumption that deviation in individual measurements within a region owes purely to

random scatter about an ideal mean value.

Our final uncertainty estimate is then each of these uncertainty terms added in quadrature. During this process, we scale the data offset uncertainty contributions from each of the properties with a deep water P18S adjustment (as given in Table 3.2) greater than the assumed measurement uncertainty (as given on the first line of Table 3.3) by the ratio of the deep water adjustment to the assumed uncertainty. Using this formulation, the largest uncertainty contribution is the uncertainty in the data offsets (~58% of the total), followed by uncertainties in the slope of the properties against density (~24%), uncertainties in the mean values of differences and model outputs for specific ranges (~7%), and uncertainties in Redfield ratios and hard vs. soft tissue pump rates (~11%).

3.4 Results and Discussion

Property differences— Property changes along isobars and isopycnals are plotted from 40 to 65° S and from 400 to 2000 m depth Figures 3.3 and 3.4. Figure 3.2 indicates the locations of isopycnals and isobars in the earlier interpolated datasets. Average values of changes for the regions considered (and their associated 95% confidence intervals) are given in Table 3.5. Here we discuss changes found along isobars and isopycnals and their likely causes. Changes along both of these coordinates are complicated by the possibility that a difference will be obtained between two distinct water masses. For isobars, changes in the circulation patters can lead to vertical displacement of water masses between the two records. For isopycnals, heat or freshwater exchange can change the density of a water mass such that it is equivalent to the density of a deeper or shallower water mass in the earlier dataset. *Bindoff and*

McDougall [1994] provide a detailed description of the complex effects of heat and

freshwater exchange along isopycnals.

Table 3.5 Regional property difference averages and 95% confidence intervals on the mean values for the regions indicated in Table 3.2.

Region	Depth [m]	Θ [°C]	S	$[O_2]$*	$[Si(OH)_4]$*	$[NO_3^-]$*	$[PO_4^{3-}]$*	A_T*	C_T*
Isopycnals									
A	77	0.002	0.000	−7.9	0.43	0.78	9.5	−1.0	77
	± 14	± 0.031	± 0.005	± 2	± 0.23	± 0.16	± 0.9	± 0.4	± 14
B	−111	0.020	0.002	−0.7	−0.54	−0.22	−0.7	−1.5	−111
	± 9	± 0.005	± 0.001	± 0.2	± 0.11	± 0.03	± 0.2	± 0.2	± 9
C	41	−0.050	−0.009	−12.2	1.37	1.18	13.4	2.7	41
	± 11	± 0.03	± 0.005	± 1.6	± 0.44	± 0.18	± 1.1	± 0.9	± 11
D	−39	−0.015	−0.003	0.5	−0.77	0.23	3.3	−0.5	−39
	± 11	± 0.008	± 0.001	± 0.4	± 0.23	± 0.07	± 0.5	± 0.5	± 11
Isobars									
E	−	0.309	0.006	−0.5	−2.65	−0.52	−0.05	0.0	−3.4
		± 0.057	± 0.004	± 1	± 0.57	± 0.15	± 0.01	± 1.3	± 0.5
F	−	−0.090	0.035	−3.7	3.47	−0.20	−0.03	4.4	3.6
		± 0.038	± 0.008	± 1.8	± 1.04	± 0.19	± 0.01	± 1.9	± 0.7
G	−	0.057	−0.016	−5.9	−0.08	0.52	0.01	9.9	1.1
		± 0.023	± 0.003	± 1.5	± 0.38	± 0.16	± 0.02	± 0.9	± 0.7
H	−	0.072	0.005	−7.7	0.56	0.37	0.01	7.9	2.8
		± 0.022	± 0.002	± 1.3	± 0.5	± 0.15	± 0.01	± 0.9	± 1
I	−	−0.125	0.040	−5.6	4.66	0.49	0.05	8.9	3.6
		± 0.046	± 0.011	± 2.7	± 1.61	± 0.25	± 0.02	± 2.9	± 1.8

* units are $\mu mol\ kg^{-1}$

Changes north of the SAF—We first consider changes along isopycnals less

dense than 27.5 kg m^{-3}, above 500 m depth, and in the regions north of 54° S for P16S

and north of 55° S for P18S (regions A and C in Figure 3.2). Isopycnal differences in

this region indicate a decrease in oxygen, an increase in nutrients, a mixed change in

salinity, and a deepening of the isopycnals themselves. Each of these observations is

consistent with a continuation of published warming and freshening trends found for the
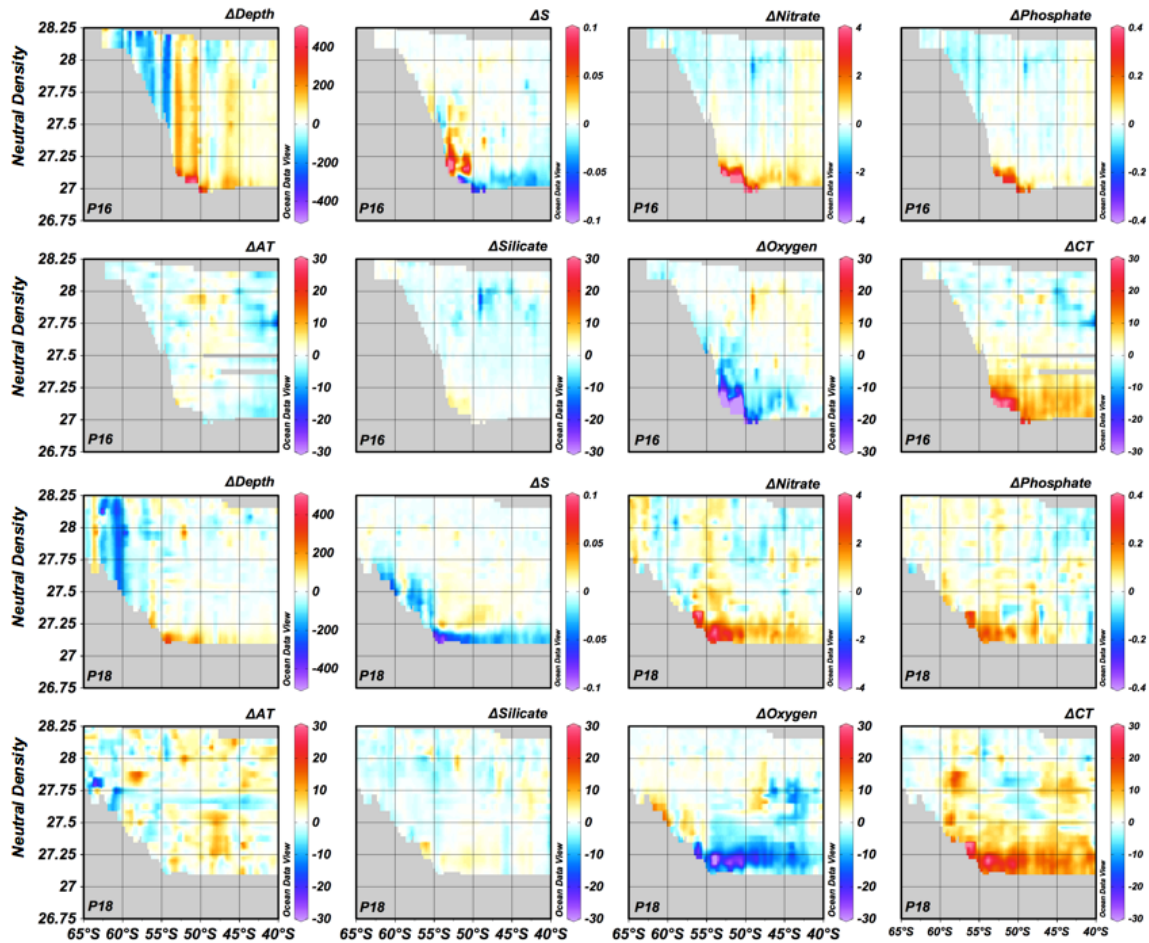
Figure 3.3 Property differences between datasets collected along section P16 (top 8 graphs) and P18 (bottom 8) and interpolated along isopycnals. Units are in °C for temperature, and μmol kg^{-1} for all others except salinity (which is unit-less). Grey areas indicate the absence of interpolated data. Triangles above the plots indicate the average latitude of the SAF (Blue), PF (Red), and SACCF (Purple). The SACCF is not displayed for P18.

source waters of AAIW and SAMW in the Indian and Pacific Oceans [*Johnson and* Orsi, 1997; *Wong et al.*, 2001; *Aoki et al.*, 2005; *Böning et al.,* 2008]. Nutrients and oxygen concentrations along isopycnals are changed by warming and freshening through the deepening of the density surfaces into less recently-ventilated waters. The change from an increase in salinity at depth to a decrease in shallower waters likely results from the salinity minimum of the AAIW mass. Above this feature, warming and freshening

isopycnals are driven deeper to lower salinity waters. Below this feature the reverse is true.

Observed changes along isobars north of the SAF are less consistent between sections than changes along isopycnals. North of 54° S along P16S (including region E), surfaces show evidence of warming and freshwater removal (or salination) at depths above 750 m with freshening extending below to ~2000 m. Additionally, there are
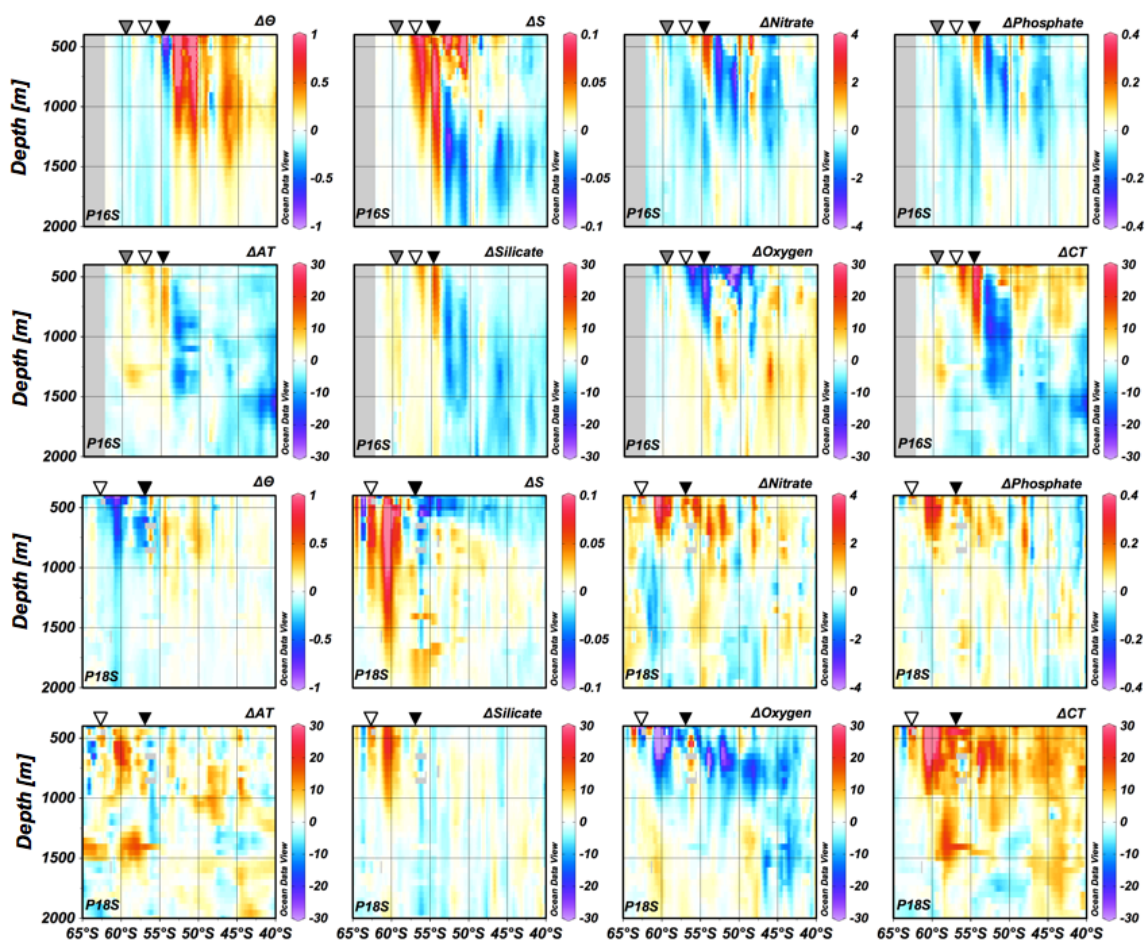

Figure 3.4 Property differences between datasets collected along section P16 (top 8 graphs) and P18 (bottom 8) and interpolated along isobars. Units are in °C for temperature, and μmol kg^{-1} for all other properties except the unit−less salinity. Grey areas indicate the absence of interpolated data.

decreases observed in nutrients and A_T, mixed changes in C_T, and a slight decrease in oxygen at shallow depths with increases below. North of 54° S along P18S (regions G and H), there is evidence of salinity decreases above 750 m with slight increases seen below extending to ~1500 m. Widespread C_T increases and oxygen decreases are found above 1500 m. There is no clear pattern in alkalinity changes. The largest changes in temperature and salinity in this region of P16S reflect warming of ~0.09 °C yr^{-1} and freshening of 0.008 yr^{-1}, or approximately 10 times the annual rate of warming found for the ACC frontal region since the 1980s by *Böning et al.* [2008]. The simplest way to account for this large discrepancy is to invoke a local deepening of gyre waters at these latitudes along P16S bringing warmer, fresher, and less-nutrient laden waters to deeper isobars. This is also consistent with the pronounced deepening of isopycnals found for this region of P16S.

Changes south of the SAF—Changes in properties interpolated along isopycnals south of the SAF (regions B and D) are less pronounced than those further north, but the isopycnals themselves are found to shoal considerably. This is consistent with heaving of waters south of the SAF. In these regions there is an indication of warming and salination of isopycnals along P16S and cooling and freshening along isopycnals along P18S. *Aoki et al.* [1995] find evidence of warming and salination along isopycnals south of the polar front in the Indian Ocean, which they consider to be symptomatic of mixing with warmer and fresher surfaces waters.

Property changes along isobars in P16S south of 54 °S (region F) indicate cooling, salination, decreases in nitrate and phosphate, increases in alkalinity and silicate, and mixed changes in oxygen and C_T. In the northern edge of this region shallower than

1000 m there is also an area with a large increase in nitrate, phosphate, silicate, C_T, and

A_T concentrations, and large decreases in oxygen concentrations and temperature. The

same patterns are found along P18S south of 58 °S (region I). The northern extema likely

represent local maxima in changes in upwelling patterns caused by localized eddies or a

northward shift in the front itself. The locations of the fronts are variable to within

several degrees [*Moore et al.*, 1999] and the steeply sloped isopycnals ensure that a small

change in the latitude of these fronts could induce a large property change between the

datasets.

Table 3.6 Average model outputs for the regions indicated in Figure
3.2. Positive residuals indicate that the data exceeded the model's
estimated value for that property. Values are given in grey when the
change is smaller than the uncertainty.

Region	Δz	Δbio	Δf	Δh	ΔgO	ΔgC
E	-0.049	3.4	-0.008	-0.095	0.8	1.6
	± 0.025	± 4.2	± 0.017	± 0.245	± 8.8	± 6.8
F	0.035	-1.3	0.008	0.003	-4.2	3.0
	± 0.015	± 2.2	± 0.011	± 0.049	± 5.7	± 5.7
G	0.012	-0.4	-0.012	0.158	-4.5	9.3
	± 0.031	± 4.8	± 0.012	± 0.271	± 8.1	± 6.7
H	0.010	-0.2	0.003	0.136	-6.0	5.8
	± 0.015	± 3	± 0.005	± 0.102	± 5.7	± 5.7
I	0.038	0.7	0.001	-0.066	3.6	0.5
	± 0.023	± 2.6	± 0.022	± 0.103	± 8.5	± 7.2

Model results— Average values and uncertainty ranges (see the uncertainty

assessment section) for model outputs are given for each region in Table 3.6. As can be

seen, the majority of the estimated trends are smaller in magnitude than their

uncertainties. Nevertheless, the few robust model outputs tell a story that is largely

consistent with the trends suspected from the changes along isopycnals and isobars and

from similar investigations [*Aoki et al*, 2005; *Böning et al,* 2008]. The dominant feature

of these outputs is the comparatively large Δz terms accounting for the majority of the temperature and salinity changes through upward displacement of water masses south of the SAF along both sections (regions F and I) and downward displacements to the north of this feature along P16S (region E).

Along P18S model outputs indicate long-term freshening (-0.0009 ± 0.0009 yr^{-1}) in the SAMW region (region G) and warming (0.010 ± 0.007 °C yr^{-1}) in the AAIW region (region H). These trends are indistinguishable from the ones published for a similar depth range of the adjacent frontal region of the ACC by *Böning et al.* [2008].

The model also suggests a long-term uptake of C_T into the SAMW mass (0.7 ± 0.5 µmol kg^{-1} yr^{-1}) and, perhaps, into the AAIW mass (0.4 ± 0.4 µmol kg^{-1} yr^{-1}). This C_T increase is likely the result of the atmospheric accumulation of anthropogenic CO_2 over this time period. The trend seems to be acting against a decrease in the overall degree of AAIW ventilation evidenced by an estimated decrease in the oxygen exchange into AAIW (-0.4 ± 0.4 µmol kg^{-1} yr^{-1}). This observation of decreased AAIW ventilation is consistent with the saturation of the Southern Ocean CO_2 sink proposed by *Le Quéré et al.* [2007], though, with only one observation of this difference, this pattern could also be produced by shorter term or cyclical trends.

Collectively, the deepening of isopycnals and water masses north of the SAF and shoaling south of the SAF imply an increase in the tilt of isopycnals across the ACC. This increase in tilt of isopycnals is a common prediction of coarse-resolution climate models that is not shared by higher-resolution models capable of resolving eddy transport [*Böning et al.*, 2008]. These observations suggest that the predicted increases in Ekman fluxes (owing to the increased strength of the atmospheric westerlies) are not being

completely mitigated by similar increases in eddy-return fluxes, as has been proposed. It is not clear whether these observations of increased isopycnal tilt are symptomatic of a global trend or simply of the limited number of sampling of locations and times employed in this study, however. *Böning et al.* [2008] find no evidence of cross-ACC isopycnal steepening in their analysis of a dataset with a much more complete temporal sampling. The large volume of datasets becoming available as the CLIVAR data collection effort completes should prove instrumental in determining whether this trend is persistent or widespread.

3.5 Conclusions

Differences between interpolations along isopycnals and isobars indicate warming and freshening in mode and intermediate waters found north of the SAF. These patterns are consistent with trends found in older observations of the Southern Ocean [*Johnson and Orsi*, 1997; *Bindoff and McDougall*, 2000; *Wong et al.*, 2001; *Aoki et al.*, 2005; *Böning et al.*, 2008] and predicted by global circulation models [*Banks and Bindoff*, 2002; *Downes et al.*, 2009]. We find evidence of shoaling of isopycnals south of the SAF along 150° W and 103° W and deepening of isopycnals to the north of the SAF along 150° W. This indicates a regional steepening of isopycnals along both sections, though it is not clear whether this is the result of limited sampling or is instead symptomatic of increased upwelling and northward Ekman advection of UCDW (as has been predicted by course-resolution circulation models).

Our application of an optimum-multiparameter model to interpolation differences for several properties allows estimation of the magnitude of these trends from otherwise

ambiguous changes. We use this model to estimate values of long term changes in AAIW and SAMW that are indistinguishable from similar trends obtained from data with significantly greater temporal and spatial resolution.

Sensitivity analysis of the inverse model to its numerous inputs suggests that the model's large output uncertainties are significantly reduced with increased data confidence. We therefore recommend a continued emphasis on collecting the highest quality and data density datasets feasible. This approach is especially dependent upon the coverage and accuracy of nutrient and alkalinity measurements. The technique would therefore perhaps benefit from alkalinity measurements being made even in the absence of C_T and the development of nutrient reference materials.

3.6 Acknowledgements

References for Chapter 3

Aoki, S., N. L. Bindoff, and J. A. Church (2005), Interdecadal water mass changes in the Southern Ocean between 30° E and 160° E, *Geophys. Res. Lett., 32*, L07607.

Banks, H. T. and N. L. Bindoff (2003), Comparison of Observed Temperature and Salinity Changes in the Indo-Pacific with Results from the Coupled Climate Model HadCM3: Processes and Mechanisms, *J. Clim., 16*, 156-166.

Böning, C. W., A. Dispert, M. Visbeck, S. R. Rintoul, and F. U. Schwarzkopf (2008), The response of the Antarctic Circumpolar Current to recent climate change, *Nature Geoscience, 1*, 864-869.

Downes, S. M., N. L. Bindoff, and S. R. Rintoul (2009), Impacts of climate change on the subduction of mode and intermediate water masses in the Southern Ocean, *J. Clim., 22*, 3289-3302.

Gnanadesikan, A., J. L. Russell, and F. Zeng (2007), How does ocean ventilation change under global warming?, *Ocean Science, 3*, 43-53.

Held, I. M. and B. J. Soden (2006), Robust responses of the hydrological cycle to global warming, *J. Clim., 19*, 5686-5699.

Jackett, D. R. and T. J. McDougall (1997), A neutral density variable for the world's oceans, *J. Phys. Oceanogr., 27*, 237-263.

Johnson, G. C. and A. H. Orsi (1997), Southwest Pacific Ocean Water-Mass Changes between 1968/69 and 1990/91*, *J. Clim., 10*, 306-316.

Key, R. M., A. Kozyr, C. L. Sabine, K. Lee, R. Wanninkhof, J. L. Bullister, R. A. Feely, F. J. Millero, C. Mordy, and T. H. Peng (2004), A global ocean carbon climatology: Results from Global Data Analysis Project (GLODAP), *Global Biogeochem. Cycles, 18*, GB4031.

Law, R. M., R. J. Matear, and R. J. Francey (2008), Comment on "Saturation of the Southern Ocean CO_2 sink due to recent climate change" (1) Peer reviewed article.

Le Quéré, C., C. Rodenbeck, E. T. Buitenhuis, T. J. Conway, R. Langenfelds, A. Gomez, C. Labuschagne, M. Ramonet, T. Nakazawa, and N. Metzl (2007), Saturation of the Southern Ocean CO_2 sink due to recent climate change, *Science, 316*, 1735.

Lenton, A. and R. J. Matear (2007), Role of the Southern Annular Mode (SAM) in Southern Ocean CO_2 uptake, *Global Biogeochem. Cycles, 21*, GB2016.

Lovenduski, N. S., N. Gruber, and S. C. Doney (2008), Toward a mechanistic understanding of the decadal trends in the Southern Ocean carbon sink, *Global Biogeochem. Cycles, 22*, GB3016.

Lovenduski, N. S., N. Gruber, S. C. Doney, and I. D. Lima (2007), Enhanced CO2 outgassing in the Southern Ocean from a positive phase of the Southern Annular Mode, *Global Biogeochem. Cycles, 21*, GB2026.

Moore, J. K., M. R. Abbott, and J. G. Richman (1999), Location and dynamics of the Antarctic Polar Front from satellite sea surface temperature data, *Journal of Geophysical Research, 104*, 3059-3073.

Orsi, A. H. and T. Whitworth (1995), On the meridional extent and fronts of the Antarctic Circumpolar Current, *Deep Sea Research Part I: Oceanographic Research Papers, 42*, 641-673.

Russell, J. L. and A. G. Dickson (2003), Variability in oxygen and nutrients in South Pacific Antarctic Intermediate Water, *Global Biogeochem. Cycles, 17*, 1033.

Sabine, C. L., R. A. Feely, N. Gruber, R. M. Key, K. Lee, J. L. Bullister, R. Wanninkhof, C. S. Wong, D. W. R. Wallace, and B. Tilbrook (2004), The oceanic sink for anthropogenic CO_2, *Science, 305*, 367-371.

Sarmiento, J. L., T. M. C. Hughes, R. J. Stouffer, and S. Manabe (1998), Simulated response of the ocean carbon cycle to anthropogenic climate warming, *Nature, 393*, 245-249.

Sloyan, B. M. and S. R. Rintoul (2001), The Southern Ocean Limb of the Global Deep Overturning Circulation, 143-173.

Speer, K., S. R. Rintoul, and B. Sloyan (2000), The Diabatic Deacon Cell*, *J. Phys. Oceanogr., 30*, 3212-3222.

Thompson, D. W. J. and S. Solomon (2002), Interpretation of recent Southern Hemisphere climate change, *Science, 296*, 895-899.

Wong, A. P. S., N. L. Bindoff, and J. A. Church (2001), Freshwater and heat changes in the North and South Pacific Oceans between the 1960s and 1985–94.

Zickfeld, K., J. C. Fyfe, M. Eby, and A. J. Weaver (2008), Comment on "Saturation of the Southern Ocean CO_2 Sink Due to Recent Climate Change", *Science, 319*, 570.